Apportionment and Inventory Optimization of Agriculture and Energy Sector Methane Emissions using Multi-month Trace Gas Measurements in Northern Colorado

Griffin J. Mead,[1] Daniel I. Herman,[1,2] Fabrizio R. Giorgetta,[1,2] Nathan A. Malarich,[1] Esther Baumann,[1,2] Brian R. Washburn,[1] Nathan R. Newbury,[1] Ian Coddington,[1] Kevin C. Cossel[1,*]

[1] National Institute of Standards and Technology, Spectrum Technology and Research Division, Boulder, CO 80305

[2] University of Colorado, Boulder, Department of Physics, Boulder, CO 80309

Corresponding author: Kevin Cossel (kevin.cossel@nist.gov)

Key Points:

- A dynamic linear model apportions energy and agriculture methane emissions from multi-month trace gas measurements in Northern Colorado
- An estimated 0.4 ± 0.2 kg CH_4 are emitted per barrel of oil equivalent produced, yielding a region-wide emission rate of 15 Mg CH_4/hr
- Optimized agriculture methane emissions are higher than inventory predictions, in part due to mislocated fluxes in the inventory.

Abstract

Quantifying sector-resolved methane fluxes in complex emissions environments is challenging yet necessary to improve emissions inventories and guide policy. Here, we separate energy and agriculture sector emissions using a dynamic linear model analysis of methane, ethane, and ammonia data measured at a Northern Colorado site from November 2021 to January 2022. By combining these sector-apportioned observations with spatially resolved inventories and Bayesian inverse methods, energy and agriculture methane fluxes are optimized across the study's ~850 km^2 sensitivity area. Energy sector fluxes are synthesized with previous literature to evaluate trends in energy-sector methane emissions. Optimized agriculture fluxes in the study area were 3× larger than inventory estimates; we demonstrate this discrepancy is consistent with differences in the modeled vs. real-world spatial distribution of agricultural sources. These results highlight how sector-apportioned methane observations can yield multi-sector inventory optimizations in complex environments.

Plain Language Summary

Improving our knowledge of the locations, magnitudes, and types of methane sources is important for implementing effective emissions mitigation technologies and regulations. Methane emissions are often challenging to quantify because a wide variety of sources can emit methane, and these disparate sources are often intermingled. We demonstrate how a dynamic linear model can use multi-month time series of two tracer gases, ethane and ammonia, to effectively separate methane emissions from the energy and agriculture sectors. Incorporating

these data into a Bayesian inverse analysis refines the magnitude and distribution of methane fluxes from each sector. Our analysis reveals that methane from agriculture is several times higher than inventory estimates. While this is in part due to the spatial distribution of sources, more monitoring is needed to improve agriculture emissions factors. Energy sector emissions factors optimized in this work are consistent with other regional studies of energy sector methane emissions. A synthesis of these works demonstrates a regional decline in energy sector emissions despite a concomitant increase in oil and gas extraction; however, current emissions are similar to 2008 estimates.

1 Introduction

Methane has ~30× greater global warming potential than carbon dioxide over a 100-year timescale. United States methane inventories estimate that the energy and agriculture sectors each contribute about a third to total U.S. anthropogenic methane emissions (Maasakkers et al., 2016). Refining energy and agriculture inventories is an important step towards identifying emissions reduction strategies. However, energy and agriculture infrastructure are often present in the same areas, which creates difficulty accurately apportioning methane emissions to each sector. Observational studies must overcome this attribution hurdle when optimizing emissions from these two important sectors.

Here, we use tracer gas measurements to constrain energy and agriculture methane emissions in a 850 km^2 area of Northern Colorado. This region is characterized by large livestock developments intermingled with tens of thousands of oil and natural gas wells exploiting the Wattenberg Field (WF), and thus presents a significant inventory optimization challenge (Figs 1a,b). We quantified methane, ethane (an energy emissions tracer), and ammonia (an agriculture tracer) mixing ratios (Fig 1c) using an open-path, mid-infrared dual-comb spectrometer (MIR-DCS) (Coddington et al., 2016; Giorgetta et al., 2021; Ycas et al., 2018) and a cavity ring-down spectrometer (CRDS). Our multi-month times series captured significant temporal variations in the correlations between methane and the tracer gases. While expected, this property required applying a dynamic linear model analysis to the data, in contrast to the more common static linear regression employed by other studies with hour-to-day length observations (Kille et al., 2019; Pollack et al., 2022; Yacovitch et al., 2014, 2015). Accurately modeling the broad distributions of these tracer gas coefficients is necessary to reliably apportion methane to the energy and agricultural sectors. A Bayesian inversion then used the DLM-derived energy and agriculture-sector methane observations and an atmospheric transport model to optimize energy and agriculture methane inventory fluxes within the study's 850 km^2 area of sensitivity (for derivation of the sensitivity area, see Section 2.5)

Results from the energy sector are synthesized with previous regional measurements and historical data. Since the first study of WF energy emissions in 2008, barrel of oil equivalent (BOE) energy production within both the study's sensitivity area and the larger WF has increased several-fold while emissions have slightly decreased. This trend is the result of declining mean WF emissions factors (EFs), which, after dropping 2.9±0.4 kg CH_4/BOE (~75%) between 2008 and 2017 have stagnated at ~0.4±0.2 kg CH_4/BOE since. As a consequence, further WF production increases may yield increasing methane emissions. In contrast, inferred agricultural methane fluxes were 3× greater than inventory estimates. We demonstrate that this

discrepancy arises partially from the spatial distribution of livestock which is not captured in the inventory model. Our work highlights that tracer gas measurements can separate emissions from different sectors even in complex emissions environments while avoiding sectoral misallocation, and reinforces the importance of further monitoring to refine inventory models as EFs change.

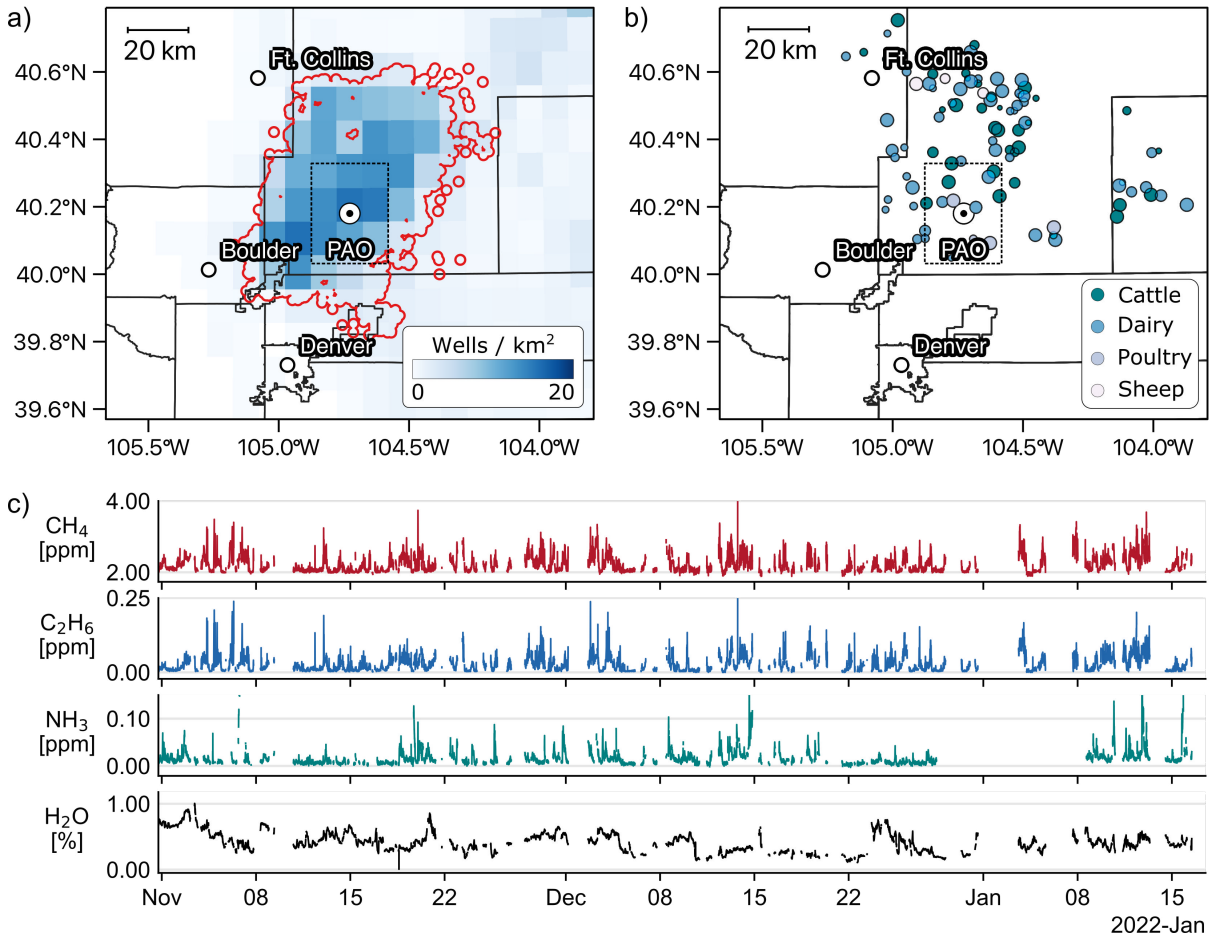

Figure 1. Energy and agriculture sector methane sources are intermingled around the Platteville Atmospheric Observatory (PAO) measurement site. The study's sensitivity area is outlined in the black dashed rectangle centered on PAO, while county borders are outlined in black. a) Thousands of wellheads (shown as a density map) extract oil and gas from the Wattenberg Field (WF, red outline). Locations of other down-stream components of the extraction process are not shown. This work's sensitivity area covers ~19% of the WF. b) Major agricultural developments called concentrated animal feeding operations (CAFOs, color coded by livestock and scaled to relative expected emissions magnitude), are widely distributed and spatially overlapped with energy infrastructure. c) The full multi-month methane, ethane, ammonia, (expressed as dry mixing ratios) and water time series recorded at PAO.

2 Materials and Methods

First we discuss the collection of time series methane and tracer gas data, and subsequent sector apportionment using a dynamic linear model. Next, we give a brief description of the atmospheric transport model and sector-resolved emissions inventory used in this work. Finally, we describe the Bayesian inversion approach which generates the optimized posterior emissions inventories.

2.1 Observational data collection

Methane (CH_4), ethane (C_2H_6), and water (H_2O) concentrations were measured at the Platteville Atmospheric Observatory (PAO, {40.182, -104.725}) from 1 November 2021 to 17 January 2022 with an open-path MIR-DCS instrument; ammonia (NH_3) was measured with a commercial CRDS. (While two instruments were used in this work, in the future all three gases could be measured using a single DCS instrument with adequate spectral coverage (Herman et al., 2021).) Figure 1c shows the dry air CH_4, C_2H_6, and NH_3 mole fraction time series reported in ppm ([μmol/mol]). Subsequent analysis relies on periods when all three species were measured. The study's estimated sensitivity area (black dashed rectangles, Figure 1a,b) encompasses 850 km^2 around PAO and denotes the area within which measurements could substantially constrain methane emissions. Further information on the DCS system and experimental setup at PAO are provided in Texts S1 and S2.

2.2 Dynamic linear model tracer gas analysis

Energy and agriculture contributions in a methane time series can be extracted using correlations with ethane and ammonia (Kille et al., 2019). Generally this is achieved by fitting the methane data to a linear regression model comprised of energy sector methane ($y_{\mathrm{Energy}} = \beta_1 [C_2H_6]$), agricultural sector methane ($y_{\mathrm{Agri}} = \beta_2 [NH_3]$), a background term ($\beta_0$), and a Gaussian noise term (ϵ):

$$[CH_4] = \beta_0 + \beta_1[C_2H_6] + \beta_2 [NH_3] + \epsilon$$

This model is appropriate here because the majority of methane emissions within the study's sensitivity area are from energy and agriculture. While landfills emit substantial volumes of methane, estimated landfill fluxes within this work's sensitivity area are <1% of predicted contributions from energy and agriculture (Text S3).

Fluctuations in the β_0, β_1, and β_2 tracer gas coefficients are expected; the background methane concentration β_0 varies diurnally as the boundary layer height changes, and the two tracer gas coefficients, β_1 and β_2, change as different sources are transported to PAO. Since a static linear regression cannot model all such variations without sub-dividing the ~2-month time series into arbitrarily smaller segments, we instead perform the tracer gas analysis using a dynamic linear model (West & Harrison, 1997). Methane data are modelled with the observation equation,

$$[CH_4]_t = F_t'\theta_t + \nu_t, \qquad \nu_t \sim N[0, V_t],$$

and the system equation,

$$\theta_t = \theta_{t-1} + \omega_t, \qquad \omega_t \sim N[0, W_t],$$

where t is an index representing data time steps. Tracer gas observations, along with a constant unity term which models the intercept, are represented by the regression vector $F_t = (1, [C_2H_6]_t, [NH_3]_t)$. Observations are assumed to be subject to Gaussian noise ν_t with a mean of zero and a variance V_t (defined here as the variance of the point-wise difference of the methane time series). The state vector $\theta_t = (\beta_{0,t}, \beta_{1,t}, \beta_{2,t})$ evolves over time as a function of the θ_{t-1} state vector and the evolution variance vector W_t. Because the variance is difficult to directly estimate and may not be time-invariant, DLMs are often solved using a discount factor δ instead as a proxy for the "memory" of the system over time (West & Harrison, 1997). The discount factor is defined as $\delta = P_t/(W_t + P_t)$, where P_t is the prior variance corresponding to a state vector with zero stochastic change ($W_t = 0$). In that limiting case, $\delta = 1$ (irrespective of the actual value of P_t) and the DLM is identical to a static linear regression model. An optimal discount factor can be determined through minimizing the model's mean standard error, but in practice this minimization becomes expensive for large data sets such as ours. Instead, 100 DLM fits were performed over the full times series data with discount factors sampled from a random uniform distribution spanning [0.98,0.999]; the mean values from the 100 DLM fits are used throughout. (Discount values below 0.98 lead to numerical instability; data where the fractional variance of either β_1 or β_2 was greater than 100% of the fit value are excluded in subsequent analysis. DLM-derived β_0 were consistent with region-wide background methane concentrations; see Text S4)

2.3 Atmospheric transport modelling

Influence footprints in a 6°×6° domain centered on PAO were calculated with the STILT-R atmospheric transport model and 3-km High Resolution Rapid Refresh (HRRR) meteorological data (Benjamin et al., 2016; Fasoli et al., 2018; Lin, 2003). Each influence footprint $H(z_r, T_r | z_i, T_i)$ (units of [ppm m^2 s / μmol CH_4]) connects sector-specific emissions throughout the spatial domain, at location z_i and time T_i, to observed sector-apportioned methane mixing ratios at PAO (z_r) at time T_r. Footprints were calculated for each hour in an 8-week period of observations from November and December 2021. Each footprint is the sum of a 48-hour duration back trajectory of 100 particles originating from PAO, calculated at 0.1°×0.1° resolution and hourly step size with hyper near field effects enabled.

2.4 Emissions inventories

Energy and agriculture emissions are estimated using a 0.1°×0.1° resolution sector-resolved methane inventory derived from the 2012 US EPA GHGI (Maasakkers et al., 2016). The energy sector, $\mathrm{x}_{\mathrm{Energy}}$ (units of [μmol / m^2 s]), is the sum of IPCC categories 1B2b (Natural Gas Production + Processing + Transmission + Distribution) and 1B2a (Petroleum); coal methane emissions are not considered (IPCC, 1996). The agriculture inventory, $\mathrm{x}_{\mathrm{Agri}}$, is the sum of IPCC categories 4A (Enteric Fermentation) and 4B (Manure Management).

2.5 Bayesian inversion

Sector-resolved methane time series, ($\mathrm{y}_{\mathrm{Energy}}$, $\mathrm{y}_{\mathrm{Agri}}$), can be modelled as the product of time-independent methane inventories, ($\mathrm{x}_{\mathrm{Energy}}$, $\mathrm{x}_{\mathrm{Agri}}$), and the combined set of time-varying influence footprints, H, plus an error term ϵ,

$$y_{Energy} = H\, x_{Energy} + \epsilon$$
$$y_{Agri} = H\, x_{Agri} + \epsilon$$

Bayesian inverse modelling uses observational constraints ($y^{Obs}_{Energy/Agri}$) to generate maximum a posteriori (MAP) inventory estimates, $x^{Posterior}_{Energy/Agri}$, using the prior information provided by the inventories, $x^{Prior}_{Energy/Agri}$ (Cusworth et al., 2020). The observation vector $y^{Obs}_{Energy/Agri}$ are the hourly mean mixing ratios of energy and agriculture methane averaged from the 2-minute time series. Following other studies, analysis is restricted to measurements within the hours of 11:00-16:00 local time when the simulation's boundary layer is well mixed and better captured by the meteorological models (Bianco et al., 2022; Fasoli et al., 2018; Kunik et al., 2019; McKain et al., 2015; Sargent et al., 2018). This restriction yielded a total of 238 valid data points for each observation vector. The *H* matrix contains the corresponding STILT footprint for each valid hour, where each footprint is restricted to a 5.8°×5.8° domain centered on PAO at 0.1° resolution for a total of 3422 state vector elements; footprints were flattened and stacked to yield the final *H* matrix with shape (238×3422). Variances for the diagonal prior and observational error covariance matrices were estimated using a restricted maximum likelihood (RML) approach (Michalak, 2004; Michalak et al., 2005). Analysis of the averaging kernel sensitivity matrix indicates the posterior inventory is constrained by observations in an 850 km^2 area centerd around PAO. This sensitivity area is highlighted with a dashed rectangular outline in Figures 1, 3 and 4. Further details on the inverse analysis are provided in Text S5.

3 Time-resolved sector apportioned methane

We first examine the dynamic linear model tracer gas results which provide key observational constraints for the Bayesian inversion. Three examples, shown in Figure 2, demonstrate how the DLM analysis captures how tracer gas coefficients and associated uncertainties evolve as different sources are transported to PAO. During periods with a low tracer gas concentration or little variation in the tracer gas, uncertainty in the respective coefficient increases. Additionally, an increased correlation between methane and one tracer gas reduces the respective coefficient's uncertainty.

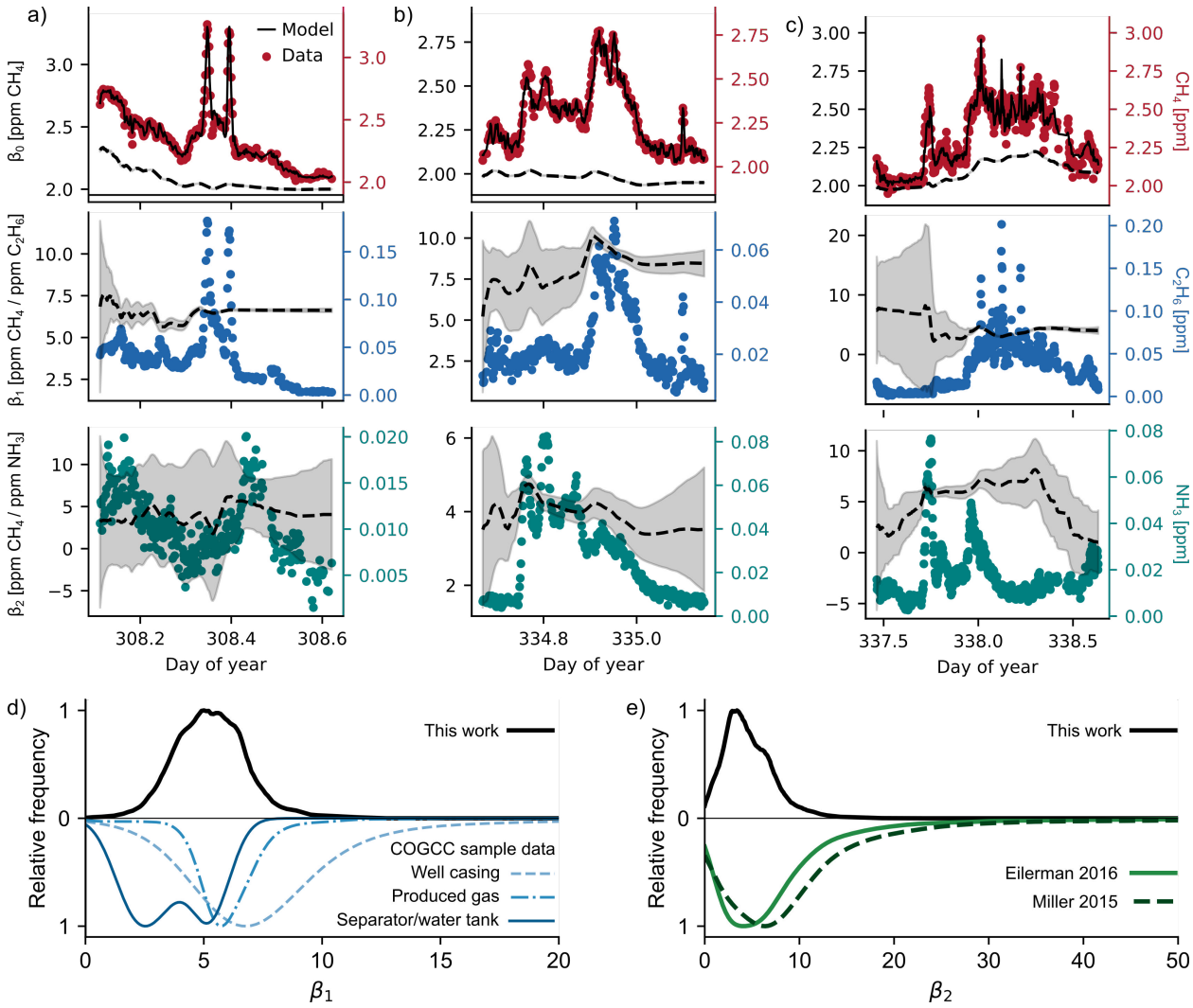

Figure 2. Three methane plumes (a,b,c) illustrate how the DLM apportions methane into contributions from the energy and agriculture sectors. The tracer gas coefficients (dashed lines, left axis) are shown with uncertainties in gray shading. In addition, the top panel shows both the full modeled methane concentration (solid line, right axis) and the measured methane concentration (red circles, right axis). The second and third rows show the ethane and ammonia measurements (colored dots, right axis). Panel d) compares the DLM-derived β_1 coefficients from the full time series with β_1 coefficients calculated from COGCC sample data. Panel e) compares β_2 coefficients at PAO with other studies performed in Northern Colorado (Eilerman et al., 2016) and California's San Joaquin Valley (Miller et al., 2015).

DLM-derived coefficients can provide insight into emission source characteristics. Figure 2d,e show kernel density estimates of the energy (β_1) and agriculture (β_2) tracer gas coefficients over the multi-month observation period. The β_1 coefficient has been observed to vary as natural gas is extracted, processed, and transported (Cardoso-Saldaña et al., 2019; Peischl et al., 2013). Ethane and methane mole fractions for natural gas samples collected after 2010 in the WF by the Colorado Oil and natural gas Conservation Commission (COGCC) provide a direct comparison to our estimates for β_1 (Figure 2d) (Colorado Oil and Gas Conservation Commission, 2022).

These data are collected from a range of sample locations, including well casings (bradenheads, well tubing, and surface, intermediate, and production casings), produced gas, and separators and water tanks. The β_1 values determined from the PAO data span the lower end of values for well casing and the higher range of values for separator and water tank emissions, but are most consistent with produced gas emissions.

Similarly, β_2 is expected to vary as emissions from different livestock species can have substantially different ratios of methane and ammonia concentrations (Golston et al., 2020). Other sources of variation could include atmospheric chemistry effects such as deposition and reactivity (primarily for NH_3). We compare our β_2 results with two mobile measurement studies in Figure 2e. While extensive sampling of ammonia/methane ratios throughout Colorado are not available, studies in both the San Joaquin Valley of California and Northern Colorado overlap well with β_2 results obtained at PAO, indicating a consistent, if broad, distribution of β_2 values for agriculture across the western United States (Eilerman et al., 2016; Miller et al., 2015).

Significant variations in tracer gas coefficients observed in this analysis emphasizes the difficulty in determining a unique set of energy and agriculture coefficients, even for measurements conducted in a single location. Despite these complexities, the DLM approach successfully generates energy and agriculture sector-apportioned methane time series ($y^{Obs}_{Energy}, y^{Obs}_{Agri}$) which provides observational constraints for inventory optimization.

4 Methane inventory optimization

In order to provide emissions estimates with quantified uncertainties, an ensemble of 100 inverse analyses were performed for each sector, with each inversion using prior and observational error variances drawn from an optimal range determined using an RML approach. Inversion results were evaluated on several metrics, including the posterior's reduced chi-squared (χ^2) value, and changes in the coefficient of determination (ΔR^2) and root mean square error (ΔRMSE) between observed (y^{Obs}) and predicted (y^{Prior} and $y^{Posterior}$) mixing ratios (Kunik et al., 2019; Tarantola, 2005). Optimal inverse results were identified as having a χ^2 close to 1 (Text S5). Finally, we compare mean fluxes from x^{Prior} and $x^{Posterior}$ within the 850 km^2 sensitivity area identified by the averaging kernel sensitivity matrix. All prior uncertainties quoted for comparison to posterior results are calculated following (Maasakkers et al., 2016). (Mean observed, prior, and posterior diurnal energy and agriculture methane mixing ratios are shown in Text S6).

4.1 Energy sector

Inverse analysis results for the energy sector are shown in Figure 3. On average, the inversions achieved a $\chi^2 = 0.98$, a RMSE reduction of 12%, and a 13% increase in R^2. Posterior mean methane fluxes within the study's sensitivity area (78 ± 33 nmol CH_4 m^{-2} s^{-1}) agree within uncertainty with the prior (100 ± 53 nmol CH_4 m^{-2} s^{-1}), although posterior emissions were slightly reduced north-east of PAO (Figure 3c). A constant error in the DCS measurement of ethane cannot account for the comparable mean prior and posterior fluxes (Text S7).

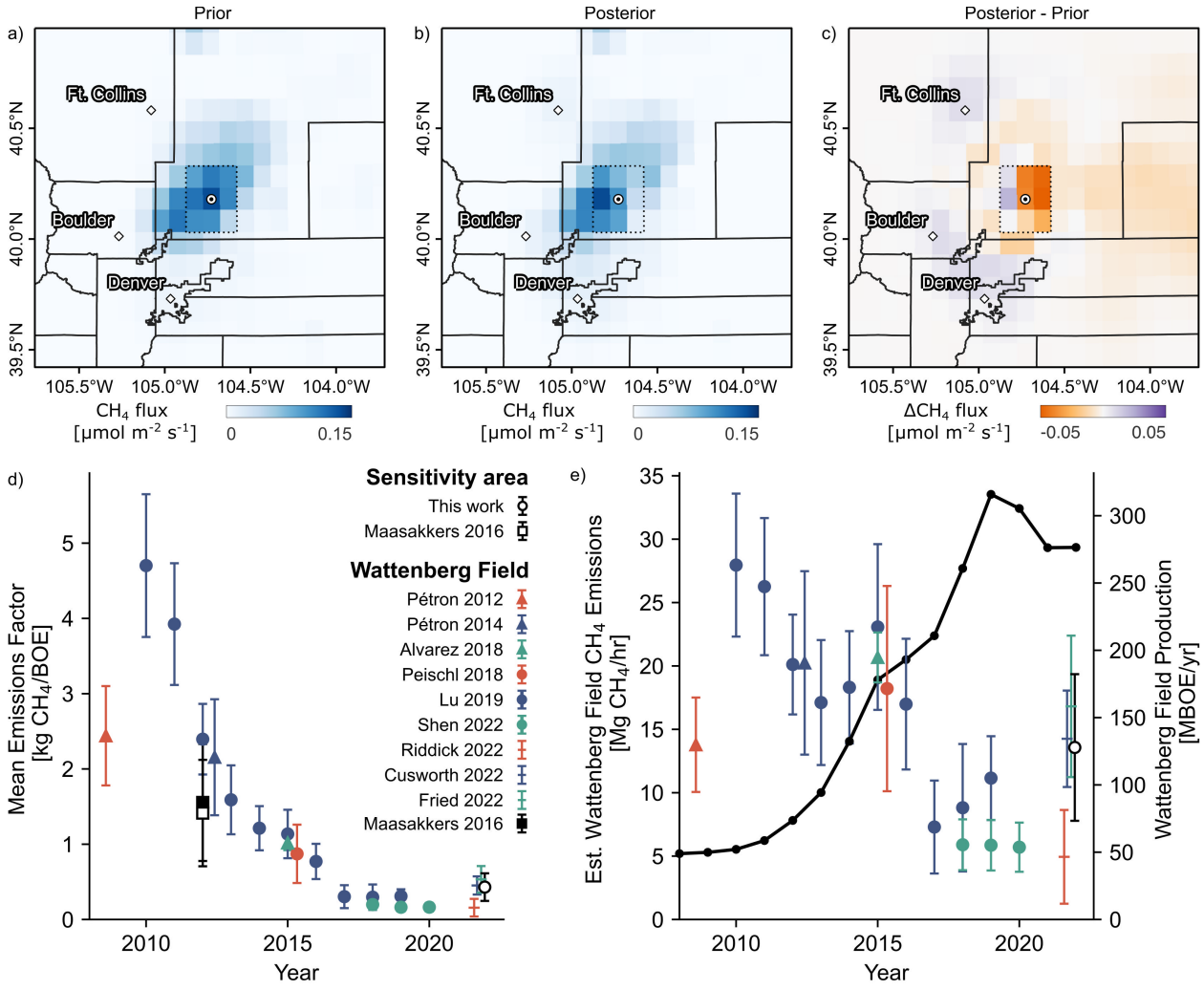

Figure 3 The spatial distribution of methane emissions from the energy sector are optimized with a Bayesian inversion using the energy sector methane time series observed at PAO. a-b) Prior (x_{Energy}^{Prior}) and posterior ($x_{Energy}^{Posterior}$) surface flux maps for energy sector methane emissions remain largely similar in both distribution and magnitude of emissions within the sensitivity region of the study area (black dashed rectangle). c) Difference between prior and posterior emissions indicate a slight reduction in emissions north-east of PAO. d) Comparison of this work's estimated mean emissions factor to other studies of the larger WF. A notable decrease in emissions factors is apparent from 2010 to 2017. e) Estimated WF methane emissions are calculated using the EFs from d) and WF energy production volumes (black line). Despite increasing production from the region, total emissions have slightly declined in the past decade.

From these results, we next calculate an EF for the study's sensitivity area. EFs quantify the amount of methane emitted by a process per volume of energy produced by that process, and are useful for generating and improving emissions inventories. Using the posterior energy flux and oil and gas production volumes within our study's 850 km^2 sensitivity area, we estimate a mean EF of 0.4 ± 0.2 kg CH_4 emitted per BOE produced (Skinner et al., 2022). For context, we also calculate historical EFs for the WF using data from multiple airplane mass balance, flask sample,

and satellite inversion studies spanning 2008 to 2021 (Alvarez et al., 2018; Cusworth et al., 2022; Fried & Dickerson, 2023; Lu et al., 2023; Peischl et al., 2018; Pétron et al., 2012, 2014; Riddick et al., 2022; Shen et al., 2022). Finally, we estimate inventory EFs for the WF and our study's sensitivity area (Maasakkers et al., 2016). Combined, this synthesis (Figure 3d, data provided in Text S8) demonstrates a clear decline in mean WF EFs from 2010 to 2017, with post-2017 EFs remaining steady. Our study, though sensitive to a smaller central region of the overall field, yields EFs consistent with the larger WF.

From this analysis, we estimate how total energy emissions have changed over time in the WF by calculating the product of each EF and the Field-wide energy production (Fig 3e). While we note that applying this work's EF to the entire Field is an extrapolation, trends in both new well installations and energy production are closely mirrored in our study's sensitivity area and the larger WF (see Text S9). A declining trend in total energy sector methane emissions since 2010 emerges from this ensemble of independent measurements, although current emissions are comparable to 2008 levels. State and federal air quality regulations likely contributed to this decline through emissions reduction regulations which likely encouraged adoption of emissions reductions technologies. Changing well infrastructure may have also contributed (Text S9). Determining the relative importance of regulations and infrastructure requires further analysis.

4.2 Agriculture sector

Results of the agriculture optimization are shown in Figure 4. The mean posterior had a $\chi^2 = 1.04$, and a RMSE reduction of 22% and a R^2 increase of 41% compared to the prior. Within the sensitivity area, fluxes around PAO increased from a prior mean of 14 ± 16 nmol CH_4 m^{-2} s^{-1} to a posterior mean of 49 ± 22 nmol CH_4 m^{-2} s^{-1} (Figure 4a,b). This 3.5× ± 2.4× increase is surprising given that the total permitted livestock population around PAO has remained roughly constant since 2012 (National Agricultural Statistics Service, n.d.). While a threefold error in livestock EFs is possible, we instead investigated whether a spatial misallocation of emissions could explain the enhanced posterior flux in the sensitivity area. A comparison of the prior (Figure 4a) to registered concentrated animal feeding operation sites (CAFOs, Figure 1b) demonstrates that fluxes are not localized around CAFOs. This is a result of methodology: the agriculture inventory was generated by probabilistically distributing county-level livestock headcounts throughout each county using multiple livestock occurence probability maps (Maasakkers et al., 2016). For some livestock, such as beef cattle which graze in pastures for parts of the year, this is a logical approach; however, poultry and dairy cattle are often on CAFOs throughout the animal's lifespan.

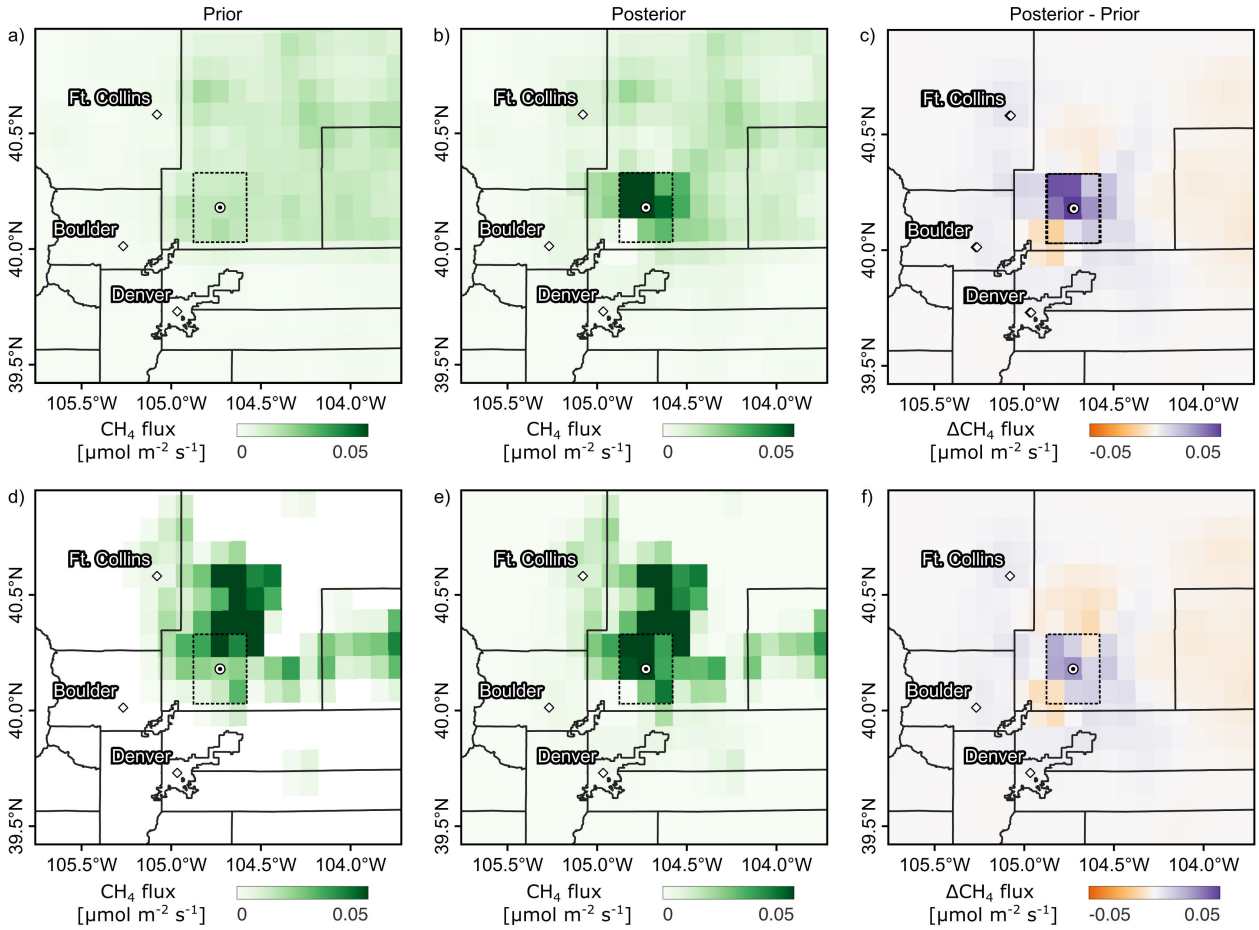

Figure 4 Comparison of agriculture-sector methane observed at PAO to the original inventory and posterior predictions (top row), and to the re-distributed inventory and posterior predictions (bottom row). a-b) Posterior ($x_{Agri}^{Posterior}$) agriculture methane within the study area's sensitivity region (black dashed rectangle) are more localized around PAO than in the prior (x_{Agri}^{Prior}). c) Difference between prior and posterior emissions are significant, with a several-fold increase in emissions to the north-west. d-e) Redistributed posterior agriculture methane is distributed similarly to the redistributed prior. f) Differences between the re-distributed prior and posterior are slight, suggesting that the re-distribution better captures the distribution of emissions around PAO.

To determine if concentrating emissions to CAFO locations improved agreement with observations, county-level inventory emissions were calculated and redistributed (Text S10) to CAFO locations within each county proportionate to the total animal equivalent emissions units at each CAFO (Golston et al., 2020). Total county level emissions were unchanged, reflecting our assumption that agricultural emissions have remained constant. The redistributed prior had a mean flux of 30 ± 34 nmol CH_4 m^{-2} s^{-1} within the sensitivity area, which increased in $x_{Redist\ Agri}^{Posterior}$ to 43 ± 29 nmol CH_4 m^{-2} s^{-1}, comparable to the original $x_{Agri}^{Posterior}$ results. The redistributed posterior had a similar χ^2 value (0.96) but a smaller RMSE reduction of 11% and a smaller R^2 increase of 25%, consistent with the smaller differences (Figure 4f) between the redistributed

prior (Figure 4d) and posterior (Figure 4e), compared to those observed with the original inventory (Figure 4c).

5 Conclusions

We constrain energy and agriculture methane emissions in a ~850 km^2 area in Northern Colorado by analyzing measurements of methane, ethane, and ammonia with a dynamic linear model and Bayesian inversion. Comparison with the 2012 gridded EPA inventory within the study area showed a small decrease in energy sector methane emissions which was consistent with a decrease in energy EFs from 2010 to 2017 observed by other studies. State and federal regulations and changing energy infrastructure likely contributed to this decline. While current energy emissions are lower than 2010 levels, they are comparable to 2008 observations, which indicates that further reductions are necessary to meet Colorado's target of 50% reduction by 2030 and 90% reduction by 2050 relative to 2005 levels. A significant increase in posterior agricultural methane emissions helped identify issues in the spatial distribution of agricultureal fluxes. Redistributing emissions to CAFO sites improved agreement between the redistributed prior and posterior, although posterior agriculture emissions in the sensitivity area remain ~50% higher than the redistributed prior. Improved spatial distribution of inventory emissions are critical for regional scale studies using aircraft or satellite observations where multiple tracer gas observations are not present (Cusworth et al., 2021; Peischl et al., 2018). While conclusions from our single-sensor study can be improved with a distributed sensor network, it is noteworthy this approach can refine sector-resolved methane emission across areas comparable to the footprints of many methane observing satellites (Cusworth et al., 2021; Ware et al., 2019).

Acknowledgments

Funding. G.M. acknowledges support from the NIST NRC fellowship program. Funding for this work was provided by NIST and the NASA Instrument Incubator Program.

Acknowledgments. The authors thank NOAA (Eric Williams) for access to the Platteville Atmospheric Observatory, Andy Neuman for loan of the ammonia CRDS instrument, and Dan Zimmerle, Dan Bon, and Chad DeVolin for CAFO information.The authors thank Newton Nguyen, Israel Lopez-Coto, Zachary Grey, and Subhomoy Ghosh for helpful suggestions and comments. Finally, the authors thank both anonymous reviewers for their constructive and knowledgable critiques of this work.

Disclosures. The authors declare no conflicts of interest.

Data availability. The time series methane, ethane, ammonia, and water mixing ratio data, the mean hourly sector-apportioned methane mixing ratio data, and the atmospheric transport matrix *H* used for Bayesian inverse analysis are available at the NIST Public Data Repository (https://doi.org/10.18434/mds2-3020) (Mead, 2023).

Open Research

The time series methane, ethane, ammonia, and water mixing ratio data, the mean hourly sector-apportioned methane mixing ratio data, and the atmospheric transport matrix $\boldsymbol{H}$ used for Bayesian inverse analysis are available at the NIST Public Data Repository (https://doi.org/10.18434/mds2-3020)

References

Alvarez, R. A., Zavala-Araiza, D., Lyon, D. R., Allen, D. T., Barkley, Z. R., Brandt, A. R., et al. (2018). Assessment of methane emissions from the U.S. oil and gas supply chain. *Science*, 186–188. https://doi.org/10.1126/science.aar7204

Benjamin, S. G., Weygandt, S. S., Brown, J. M., Hu, M., Alexander, C. R., Smirnova, T. G., et al. (2016). A North American Hourly Assimilation and Model Forecast Cycle: The Rapid Refresh. *Monthly Weather Review*, *144*(4), 1669–1694. https://doi.org/10.1175/MWR-D-15-0242.1

Bianco, L., Muradyan, P., Djalalova, I., Wilczak, J. M., Olson, J. B., Kenyon, J. S., et al. (2022). Comparison of Observations and Predictions of Daytime Planetary-Boundary-Layer Heights and Surface Meteorological Variables in the Columbia River Gorge and Basin During the Second Wind Forecast Improvement Project. *Boundary-Layer Meteorology*, *182*(1), 147–172. https://doi.org/10.1007/s10546-021-00645-x

Cardoso-Saldaña, F. J., Kimura, Y., Stanley, P., McGaughey, G., Herndon, S. C., Roscioli, J. R., et al. (2019). Use of Light Alkane Fingerprints in Attributing Emissions from Oil and Gas Production. *Environmental Science & Technology*, *53*(9), 5483–5492. https://doi.org/10.1021/acs.est.8b05828

Coddington, I., Newbury, N., & Swann, W. (2016). Dual-comb spectroscopy. *Optica*, *3*(4), 414–426. https://doi.org/10.1364/OPTICA.3.000414

Colorado Oil and Gas Conservation Commission. (2022, September 15). Oil and Gas Well Analytical Data. Retrieved from https://cogcc.state.co.us/documents/data/downloads/environmental/ProdWellDownLoad.html

Cusworth, D. H., Duren, R. M., Yadav, V., Thorpe, A. K., Verhulst, K., Sander, S., et al. (2020). Synthesis of Methane Observations Across Scales: Strategies for Deploying a Multitiered Observing Network. *Geophysical Research Letters*, *47*(7). https://doi.org/10.1029/2020GL087869

Cusworth, D. H., Bloom, A. A., Ma, S., Miller, C. E., Bowman, K., Yin, Y., et al. (2021). A Bayesian framework for deriving sector-based methane emissions from top-down fluxes. *Communications Earth & Environment*, *2*(1), 242. https://doi.org/10.1038/s43247-021-00312-6

Cusworth, D. H., Thorpe, A. K., Ayasse, A. K., Stepp, D., Heckler, J., Asner, G. P., et al. (2022). Strong methane point sources contribute a disproportionate fraction of total emissions across multiple basins in the United States. *Proceedings of the National Academy of Sciences*, *119*(38), e2202338119. https://doi.org/10.1073/pnas.2202338119

Eilerman, S. J., Peischl, J., Neuman, J. A., Ryerson, T. B., Aikin, K. C., Holloway, M. W., et al. (2016). Characterization of Ammonia, Methane, and Nitrous Oxide Emissions from Concentrated Animal Feeding Operations in Northeastern Colorado. *Environmental Science & Technology*, *50*(20), 10885–10893. https://doi.org/10.1021/acs.est.6b02851

Fasoli, B., Lin, J. C., Bowling, D. R., Mitchell, L., & Mendoza, D. (2018). Simulating atmospheric tracer concentrations for spatially distributed receptors: updates to the Stochastic Time-Inverted Lagrangian Transport model's R interface (STILT-R version

2). *Geoscientific Model Development*, *11*(7), 2813–2824. https://doi.org/10.5194/gmd-11-2813-2018

Fried, A., & Dickerson, R. R. (2023). *Continuous Airborne Measurements and Analysis of Oil & Natural Gas Emissions During the 2021 Denver-Julesburg Basin Studies*. University of Colorado Boulder. Retrieved from https://apcd.state.co.us/aqidev/tech_doc_repository.aspx?action=open&file=CU_UMD_2021_Final_Report.pdf

Giorgetta, F. R., Peischl, J., Herman, D. I., Ycas, G., Coddington, I., Newbury, N. R., & Cossel, K. C. (2021). Open-Path Dual-Comb Spectroscopy for Multispecies Trace Gas Detection in the 4.5–5 μm Spectral Region. *Laser & Photonics Reviews*, *15*(9), 2000583. https://doi.org/10.1002/lpor.202000583

Golston, L. M., Pan, D., Sun, K., Tao, L., Zondlo, M. A., Eilerman, S. J., et al. (2020). Variability of Ammonia and Methane Emissions from Animal Feeding Operations in Northeastern Colorado. *Environmental Science & Technology*, *54*(18), 11015–11024. https://doi.org/10.1021/acs.est.0c00301

Herman, D. I., Weerasekara, C., Hutcherson, L. C., Giorgetta, F. R., Cossel, K. C., Waxman, E. M., et al. (2021). Precise multispecies agricultural gas flux determined using broadband open-path dual-comb spectroscopy. *Science Advances*, *7*(14), eabe9765. https://doi.org/10.1126/sciadv.abe9765

IPCC. (1996). Emission Factor Database. Retrieved from https://www.ipcc-nggip.iges.or.jp/EFDB/find_ef.php

Kille, N., Chiu, R., Frey, M., Hase, F., Sha, M. K., Blumenstock, T., et al. (2019). Separation of Methane Emissions From Agricultural and Natural Gas Sources in the Colorado Front

Range. *Geophysical Research Letters*, *46*(7), 3990–3998. https://doi.org/10.1029/2019GL082132

Kunik, L., Mallia, D. V., Gurney, K. R., Mendoza, D. L., Oda, T., & Lin, J. C. (2019). Bayesian inverse estimation of urban CO2 emissions: Results from a synthetic data simulation over Salt Lake City, UT. *Elementa: Science of the Anthropocene*, *7*, 36. https://doi.org/10.1525/elementa.375

Lin, J. C. (2003). A near-field tool for simulating the upstream influence of atmospheric observations: The Stochastic Time-Inverted Lagrangian Transport (STILT) model. *Journal of Geophysical Research*, *108*(D16), ACH 2-1-ACH 2-17. https://doi.org/10.1029/2002JD003161

Lu, X., Jacob, D. J., Zhang, Y., Shen, L., Sulprizio, M. P., Maasakkers, J. D., et al. (2023). Observation-derived 2010-2019 trends in methane emissions and intensities from US oil and gas fields tied to activity metrics. *Proceedings of the National Academy of Sciences*, *120*(17), e2217900120. https://doi.org/10.1073/pnas.2217900120

Maasakkers, J. D., Jacob, D. J., Sulprizio, M. P., Turner, A. J., Weitz, M., Wirth, T., et al. (2016). Gridded National Inventory of U.S. Methane Emissions. *Environmental Science & Technology*, *50*(23), 13123–13133. https://doi.org/10.1021/acs.est.6b02878

McKain, K., Down, A., Raciti, S. M., Budney, J., Hutyra, L. R., Floerchinger, C., et al. (2015). Methane emissions from natural gas infrastructure and use in the urban region of Boston, Massachusetts. *Proceedings of the National Academy of Sciences*, *112*(7), 1941–1946. https://doi.org/10.1073/pnas.1416261112

Mead, G. (2023). Data for: "Apportionment and Inventory Optimization of Agriculture and Energy Sector Methane Emissions using Multi-month Trace Gas Measurements in

494 Northern Colorado" [Data set]. NIST Public Data Repository.
495 https://doi.org/10.18434/mds2-3020
496 Michalak, A. M. (2004). A geostatistical approach to surface flux estimation of atmospheric
497 trace gases. *Journal of Geophysical Research*, *109*(D14), D14109.
498 https://doi.org/10.1029/2003JD004422
499 Michalak, A. M., Hirsch, A., Bruhwiler, L., Gurney, K. R., Peters, W., & Tans, P. P. (2005).
500 Maximum likelihood estimation of covariance parameters for Bayesian atmospheric trace
501 gas surface flux inversions. *Journal of Geophysical Research*, *110*(D24), D24107.
502 https://doi.org/10.1029/2005JD005970
503 Miller, D. J., Sun, K., Tao, L., Pan, D., Zondlo, M. A., Nowak, J. B., et al. (2015). Ammonia and
504 methane dairy emission plumes in the San Joaquin Valley of California from individual
505 feedlot to regional scales. *Journal of Geophysical Research: Atmospheres*, *120*(18),
506 9718–9738. https://doi.org/10.1002/2015JD023241
507 National Agricultural Statistics Service. (n.d.). Colorado Annual Agricultural Statistics Bulletin.
508 United States Department of Agriculture. Retrieved from
509 https://www.nass.usda.gov/Statistics_by_State/Colorado/Publications/Annual_Statistical
510 _Bulletin/index.php
511 Peischl, J., Ryerson, T. B., Brioude, J., Aikin, K. C., Andrews, A. E., Atlas, E., et al. (2013).
512 Quantifying sources of methane using light alkanes in the Los Angeles basin, California:
513 SOURCES OF METHANE IN L.A. *Journal of Geophysical Research: Atmospheres*,
514 *118*(10), 4974–4990. https://doi.org/10.1002/jgrd.50413
515 Peischl, J., Eilerman, S. J., Neuman, J. A., Aikin, K. C., de Gouw, J., Gilman, J. B., et al. (2018).
516 Quantifying Methane and Ethane Emissions to the Atmosphere From Central and

Western U.S. Oil and Natural Gas Production Regions. *Journal of Geophysical Research: Atmospheres*. https://doi.org/10.1029/2018JD028622

Pétron, G., Frost, G., Miller, B. R., Hirsch, A. I., Montzka, S. A., Karion, A., et al. (2012). Hydrocarbon emissions characterization in the Colorado Front Range: A pilot study. *Journal of Geophysical Research: Atmospheres*, *117*(D4), D04304. https://doi.org/10.1029/2011JD016360

Pétron, G., Karion, A., Sweeney, C., Miller, B. R., Montzka, S. A., Frost, G. J., et al. (2014). A new look at methane and nonmethane hydrocarbon emissions from oil and natural gas operations in the Colorado Denver-Julesburg Basin. *Journal of Geophysical Research: Atmospheres*, *119*(11), 6836–6852. https://doi.org/10.1002/2013JD021272

Pollack, I. B., McCabe, M. E., Caulton, D. R., & Fischer, E. V. (2022). Enhancements in Ammonia and Methane from Agricultural Sources in the Northeastern Colorado Front Range Using Observations from a Small Research Aircraft. *Environmental Science & Technology*, *56*(4), 2236–2247. https://doi.org/10.1021/acs.est.1c07382

Riddick, S. N., Cheptonui, F., Yuan, K., Mbua, M., Day, R., Vaughn, T. L., et al. (2022). Estimating Regional Methane Emission Factors from Energy and Agricultural Sector Sources Using a Portable Measurement System: Case Study of the Denver–Julesburg Basin. *Sensors*, *22*(19), 7410. https://doi.org/10.3390/s22197410

Sargent, M., Barrera, Y., Nehrkorn, T., Hutyra, L. R., Gately, C. K., Jones, T., et al. (2018). Anthropogenic and biogenic CO_2 fluxes in the Boston urban region. *Proceedings of the National Academy of Sciences*, *115*(29), 7491–7496. https://doi.org/10.1073/pnas.1803715115

539 Shen, L., Gautam, R., Omara, M., Zavala-Araiza, D., Maasakkers, J. D., Scarpelli, T. R., et al.
540 (2022). Satellite quantification of oil and natural gas methane emissions in the US and
541 Canada including contributions from individual basins. *Atmospheric Chemistry and*
542 *Physics*, *22*(17), 11203–11215. https://doi.org/10.5194/acp-22-11203-2022
543 Skinner, C. C., Miller, R. F., Kinney, S. A., Gianoutsos, N. J., Gunther, G., & Shorten, C. M.
544 (2022). Aggregated Oil and Natural Gas Drilling and Production History of the United
545 States [Data set]. U.S. Geological Survey. https://doi.org/10.5066/P9UIR5HE
546 Tarantola, A. (2005). *Inverse Problem Theory and Methods for Model Parameter Estimation*.
547 Society for Industrial and Applied Mathematics.
548 https://doi.org/10.1137/1.9780898717921
549 Ware, J., Kort, E. A., Duren, R., Mueller, K. L., Verhulst, K., & Yadav, V. (2019). Detecting
550 Urban Emissions Changes and Events With a Near-Real-Time-Capable Inversion
551 System. *Journal of Geophysical Research: Atmospheres*, *124*(9), 5117–5130.
552 West, M., & Harrison, J. (1997). *Bayesian forecasting and dynamic models* (2nd ed). New York:
553 Springer.
554 Yacovitch, T. I., Herndon, S. C., Roscioli, J. R., Floerchinger, C., McGovern, R. M., Agnese, M.,
555 et al. (2014). Demonstration of an Ethane Spectrometer for Methane Source
556 Identification. *Environmental Science & Technology*, *48*(14), 8028–8034.
557 https://doi.org/10.1021/es501475q
558 Yacovitch, T. I., Herndon, S. C., Pétron, G., Kofler, J., Lyon, D., Zahniser, M. S., & Kolb, C. E.
559 (2015). Mobile Laboratory Observations of Methane Emissions in the Barnett Shale
560 Region. *Environmental Science & Technology*, *49*(13), 7889–7895.
561 https://doi.org/10.1021/es506352j

562 Ycas, G., Giorgetta, F. R., Baumann, E., Coddington, I., Herman, D., Diddams, S. A., &
563 Newbury, N. R. (2018). High-coherence mid-infrared dual-comb spectroscopy spanning
564 2.6 to 5.2 μm. *Nature Photonics*, *12*(4), 202–208. https://doi.org/10.1038/s41566-018-
565 0114-7

566

567

References From the Supporting Information

Alvarez, R. A., Zavala-Araiza, D., Lyon, D. R., Allen, D. T., Barkley, Z. R., Brandt, A. R., et al. (2018). Assessment of methane emissions from the U.S. oil and gas supply chain. *Science*, 186–188. https://doi.org/10.1126/science.aar7204

Benjamin, S. G., Weygandt, S. S., Brown, J. M., Hu, M., Alexander, C. R., Smirnova, T. G., et al. (2016). A North American Hourly Assimilation and Model Forecast Cycle: The Rapid Refresh. *Monthly Weather Review*, *144*(4), 1669–1694. https://doi.org/10.1175/MWR-D-15-0242.1

Boulder County Public Health, Boulder A.I.R., LLC, & Colorado Department of Public Health and Environment. (n.d.). Boulder Reservoir Atmospheric Chemical Conditions. Retrieved from https://www.bouldair.com/boulder.htm#header

City of Longmont, & Boulder A.I.R., LLC. (n.d.). Longmont Union Reservoir Atmospheric Chemical Conditions. Retrieved from https://www.bouldair.com/longmont.htm

Cusworth, D., Thorpe, A., Ayasse, A., Stepp, D., Heckler, J., Asner, G., et al. (2022). *Strong methane point sources contribute a disproportionate fraction of total emissions across multiple basins in the U.S.* (preprint). Earth Sciences. https://doi.org/10.31223/X53P88

Cusworth, D. H., Duren, R. M., Yadav, V., Thorpe, A. K., Verhulst, K., Sander, S., et al. (2020). Synthesis of Methane Observations Across Scales: Strategies for Deploying a Multitiered Observing Network. *Geophysical Research Letters*, *47*(7). https://doi.org/10.1029/2020GL087869

Fried, A., & Dickerson, R. R. (2023). *Continuous Airborne Measurements and Analysis of Oil & Natural Gas Emissions During the 2021 Denver-Julesburg Basin Studies*. University of Colorado Boulder. Retrieved from https://apcd.state.co.us/aqidev/tech_doc_repository.aspx?action=open&file=CU_UMD_2021_Final_Report.pdf

Giorgetta, F. R., Peischl, J., Herman, D. I., Ycas, G., Coddington, I., Newbury, N. R., & Cossel, K. C. (2021). Open-Path Dual-Comb Spectroscopy for Multispecies Trace Gas Detection in the 4.5–5 μm Spectral Region. *Laser & Photonics Reviews*, *15*(9), 2000583. https://doi.org/10.1002/lpor.202000583

Gordon, I. E., Rothman, L. S., Hargreaves, R. J., Hashemi, R., Karlovets, E. V., Skinner, F. M., et al. (2021). The HITRAN2020 molecular spectroscopic database. *Journal of Quantitative Spectroscopy and Radiative Transfer*, 107949. https://doi.org/10.1016/j.jqsrt.2021.107949

Gordon, I. E., Rothman, L. S., Hargreaves, R. J., Hashemi, R., Karlovets, E. V., Skinner, F. M., et al. (2022). The HITRAN2020 molecular spectroscopic database. *Journal of Quantitative Spectroscopy and Radiative Transfer*, *277*, 107949. https://doi.org/10.1016/j.jqsrt.2021.107949

Herman, D., Mead, G., Giorgetta, F. R., Baumann, E., Malarich, N., Washburn, B. R., et al. (2023). Open-path measurement of stable water isotopologues using mid-infrared dual-comb spectroscopy.

Kunik, L., Mallia, D. V., Gurney, K. R., Mendoza, D. L., Oda, T., & Lin, J. C. (2019). Bayesian inverse estimation of urban CO2 emissions: Results from a synthetic data simulation over Salt Lake City, UT. *Elementa: Science of the Anthropocene*, *7*, 36. https://doi.org/10.1525/elementa.375

Lu, X., Jacob, D. J., Wang, H., Maasakkers, J. D., Zhang, Y., Scarpelli, T. R., et al. (2022). Methane emissions in the United States, Canada, and Mexico: evaluation of national methane emission inventories and 2010–2017 sectoral trends by inverse analysis of in situ (GLOBALVIEWplus CH₄ ObsPack) and satellite (GOSAT) atmospheric observations. *Atmospheric Chemistry and Physics*, *22*(1), 395–418. https://doi.org/10.5194/acp-22-395-2022

Maasakkers, J. D., Jacob, D. J., Sulprizio, M. P., Turner, A. J., Weitz, M., Wirth, T., et al. (2016). Gridded National Inventory of U.S. Methane Emissions. *Environmental Science & Technology*, *50*(23), 13123–13133. https://doi.org/10.1021/acs.est.6b02878

Michalak, A. M., Hirsch, A., Bruhwiler, L., Gurney, K. R., Peters, W., & Tans, P. P. (2005). Maximum likelihood estimation of covariance parameters for Bayesian atmospheric trace gas surface flux inversions. *Journal of Geophysical Research*, *110*(D24), D24107. https://doi.org/10.1029/2005JD005970

Newville, Matthew, Stensitzki, Till, Allen, Daniel B., & Ingargiola, Antonino. (2014, September 21). LMFIT: Non-Linear Least-Square Minimization and Curve-Fitting for Python. Zenodo. https://doi.org/10.5281/zenodo.11813

Peischl, J., Eilerman, S. J., Neuman, J. A., Aikin, K. C., de Gouw, J., Gilman, J. B., et al. (2018). Quantifying Methane and Ethane Emissions to the Atmosphere From Central and Western U.S. Oil and Natural Gas

Production Regions. *Journal of Geophysical Research: Atmospheres*. https://doi.org/10.1029/2018JD028622

Pétron, G., Frost, G., Miller, B. R., Hirsch, A. I., Montzka, S. A., Karion, A., et al. (2012). Hydrocarbon emissions characterization in the Colorado Front Range: A pilot study: COLORADO FRONT RANGE EMISSIONS STUDY. *Journal of Geophysical Research: Atmospheres*, *117*(D4), n/a-n/a. https://doi.org/10.1029/2011JD016360

Pétron, G., Karion, A., Sweeney, C., Miller, B. R., Montzka, S. A., Frost, G. J., et al. (2014). A new look at methane and nonmethane hydrocarbon emissions from oil and natural gas operations in the Colorado Denver-Julesburg Basin. *Journal of Geophysical Research: Atmospheres*, *119*(11), 6836–6852. https://doi.org/10.1002/2013JD021272

Riddick, S. N., Cheptonui, F., Yuan, K., Mbua, M., Day, R., Vaughn, T. L., et al. (2022). Estimating Regional Methane Emission Factors from Energy and Agricultural Sector Sources Using a Portable Measurement System: Case Study of the Denver–Julesburg Basin. *Sensors*, *22*(19), 7410. https://doi.org/10.3390/s22197410

Roy, J., Deschênes, J.-D., Potvin, S., & Genest, J. (2012). Continuous real-time correction and averaging for frequency comb interferometry. *Optics Express*, *20*(20), 21932–21939. https://doi.org/10.1364/OE.20.021932

Shen, L., Gautam, R., Omara, M., Zavala-Araiza, D., Maasakkers, J. D., Scarpelli, T. R., et al. (2022). Satellite quantification of oil and natural gas methane emissions in the US and Canada including contributions from individual basins. *Atmospheric Chemistry and Physics*, *22*(17), 11203–11215. https://doi.org/10.5194/acp-22-11203-2022

Tarantola, A. (2005). *Inverse Problem Theory and Methods for Model Parameter Estimation*. Society for Industrial and Applied Mathematics. https://doi.org/10.1137/1.9780898717921

Ycas, G., Giorgetta, F. R., Baumann, E., Coddington, I., Herman, D., Diddams, S. A., & Newbury, N. R. (2018). High-coherence mid-infrared dual-comb spectroscopy spanning 2.6 to 5.2 μm. *Nature Photonics*, *12*(4), 202–208. https://doi.org/10.1038/s41566-018-0114-7

Ycas, G., Giorgetta, F. R., Cossel, K. C., Waxman, E. M., Baumann, E., Newbury, N. R., & Coddington, I. (2019). Mid-infrared dual-comb spectroscopy of volatile organic compounds across long open-air paths. *Optica*, *6*(2), 165–168. https://doi.org/10.1364/OPTICA.6.000165

Ycas, G., Giorgetta, F. R., Friedlein, J. T., Herman, D., Cossel, K. C., Baumann, E., et al. (2020). Compact mid-infrared dual-comb spectrometer for outdoor spectroscopy. *Optics Express*, *28*(10), 14740–14752. https://doi.org/10.1364/OE.385860

Geophysical Research Letters

Supporting Information for

Apportionment and Inventory Optimization of Agriculture and Energy Sector Methane Emissions using Multi-month Trace Gas Measurements in Northern Colorado

Griffin J. Mead,[1] Daniel I. Herman,[1,2] Fabrizio R. Giorgetta,[1,2] Nathan A. Malarich,[1] Esther Baumann,[1,2] Brian R. Washburn,[1] Nathan R. Newbury,[1] Ian Coddington,[1] Kevin C. Cossel[1,*]

[1] National Institute of Standards and Technology, Spectrum Technology and Research Division, Boulder, CO 80305

[2] University of Colorado, Boulder, Department of Physics, Boulder, CO 80309

Contents of this file

Introduction

This work relies upon observational time series data, meteorological model data, and surface flux data. Time series data were produced by calculating the dry mixing ratios of methane and ethane for each 2-minute averaged spectra recorded by the mid-infrared dual-comb spectrometer at PAO. Ammonia time series data was measured with a commercial cavity ring-down spectrometer. Molecular line lists were provided by HITRAN2020 (Gordon et al., 2021); spectral fitting was performed using the LMFIT Python package (Newville, Matthew et al., 2014). High Resolution Rapid Refresh (HRRR) meteorological model (Benjamin et al., 2016) data was retrieved from the National Oceanic and Atmospheric Administration's Air Resources Laboratory FTP server (ftp://ftp.arl.noaa.gov/nams). Transport modeling using the HRRR data was performed with the STILT-R package (**https://github**.com/uataq/stilt/). Surface flux data was published in Maasakkers et al, 2016. Much of the geospatial processing and plotting was performed in QGIS. The NOAA meteorological station data can be accessed here: https://psl.noaa.gov/data/obs/sites/view_site_details.php?siteID=pvl.

Text S1: Experimental setup at the Platteville Atmospheric Observatory

An overview of instrument locations at Platteville Atmospheric Observatory is shown in Figure S1a. The mid-infrared dual-comb spectrometer (MIR-DCS) system is similar to previously reported designs (Giorgetta et al., 2021; Ycas et al., 2019, 2020) and is described in more detail in another publication (Herman et al., 2023). Briefly, the instrument measures an optical bandwidth spanning 2400 cm^{-1} to 3100 cm^{-1} with 0.006 cm^{-1} spectral resolution. A gimbal-mounted 10-cm aperture transmit/receive telescope launched MIR light along a 380 m open-air path to a 12.5-cm diameter gold hollow corner-cube retroreflector mounted on a telephone pole ~5 m above ground level. The reflected light was collected by the transmit/receive telescope, detected by a thermoelectrically cooled mercury cadmium telluride detector, digitized at 200 MHz, and coherently averaged (Roy et al., 2012; Ycas et al., 2018). Path-averaged CH_4, C_2H_6, and H_2O concentrations were retrieved from the spectra using the HITRAN2020 database (Gordon et al., 2022).

The ammonia cavity ring-down spectrometer (CRDS) analyzer was housed in a nearby trailer which was offset ~50 meters perpendicular to the MIR beam path. A ~4-meter section of ¼" PTFE tubing was inserted into an equal length copper tube, which was then wrapped in heater tape. The heated sample line was connected to the CRDS analyzer and positioned so that the tube inlet sampled air ~4 meters AGL. The heater tape was regulated to maintain a temperature of ~47 ºC. Data were collected at 1 Hz and interpolated onto the 2-minute DCS time base. Meteorological data were collected by a NOAA weather station; wind statistics for PAO during the measurement period are summarized in Figure S1b.

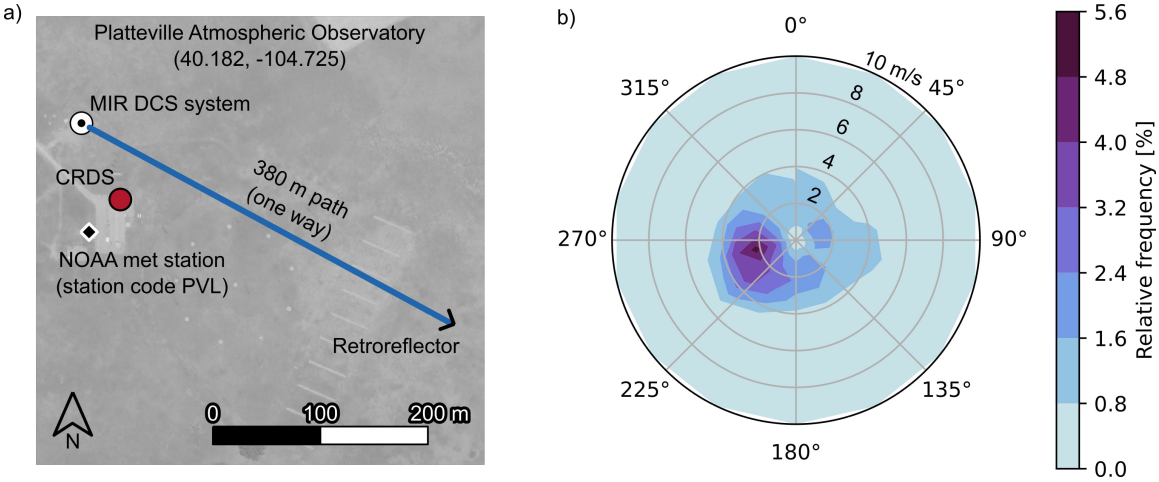

Figure S1. a) Map of instrument locations at PAO. The MIR DCS beam path traverses 380 m from a transmit/receive telescope to a retroreflector. The cavity ringdown spectrometer (CRDS) is co-located to retrieve ammonia. Satellite background image ©2023 Google and Maxar Technologies. b) Polar histogram of wind direction and speed recorded by the NOAA PVL weather station.

A key assumption of this work is that the mixing ratios of methane, ethane, and ammonia are uniform across the DCS beam path and the CRDS inlet. Any variation which does occur, for example due to venting from a nearby tank battery, is further assumed to be detected by both systems with a negligible offset in time as the plume travels from one system to the other. Depending upon the wind direction, a local plume would need to be transported 50 m-300 m

between the CRDS and DCS beam path. With a typical 2 m/s wind speed, this would result in an arrival time offset of 25-150 s, which is less than or equal to the 2-minute time base of a single data point. Therefore, the locations of the two systems are not expected to introduce any substantial error into the analysis.

Zero-air measurements were performed on the CRDS instrument every 1-2 weeks at PAO by overflowing the inlet with zero grade dry air. Across all measurements (N=10), the mean reported ammonia concentration was 1.8 ppb +/- 1.0 ppb. This concentration offset was comparable to manufacturer specifications and was subtracted from the NH_3 data prior to further analysis.

Equivalent zero-air reference measurements were not possible with the open-path DCS instrument; as a result, the reported accuracy of the methane and ethane data are estimated. For ethane, precision was estimated using a period of minimum concentration variability (4 ppb +/- 1 ppb) during the day of 31 October 2021. As listed in Table S1, concentrations measured at PAO during this time period agreed reasonably well with two independent air quality monitoring sites located at Boulder Reservoir (BRZ) (Boulder County Public Health et al., n.d.) and Longmont Union Reservoir (LUR) (City of Longmont & Boulder A.I.R., LLC, n.d.). Locations of the BRZ and LUR sites are shown in Figure S4a. From this intercomparison, we estimate the MIR DCS ethane accuracy and precision to be ±1 ppb. While this intercomparison suggests errors in the measured ethane concentrations are minimal, in Section S7 we also examine the impact a positive ethane concentration offset (equal to the mean value observed at midday on Oct 31, 2021) has on the Bayesian inverse analysis energy results.

Table S1. Mean ethane concentrations observed at PAO, LUR, and BRZ on midday Oct 31, 2021.

Site	Ethane [ppb]
PAO	4 ± 1
LUR	4.3 ± 1.5
BRZ	3.6 ± 0.5

Methane precision was determined to be ±1 ppb over the same 31 October 2021 period. Data from a CH_4 CRDS instrument collocated with the NH_3 CRDS instrument closely matched the DCS observations ($CH_4^{CRDS} = 0.994 \times CH_4^{DCS}$, $R^2 = 0.998$).

Text S2: Dual-comb spectroscopy

A basic overview of the dual-comb spectroscopy method is shown in Figure S2a. Two mid-infrared frequency combs transmit through an absorbing sample (in this case, an open-air path). Interference between the two combs on a photodiode down-converts information at optical frequencies to radio frequencies. Using known comb parameters, the optical spectrum (Figure S2b) can be reproduced from the radio signal. Methane, ethane, and water concentrations were fit in the 2918-2968 cm^{-1} spectral region for all data in this analysis. The spectral baseline was modelled with a fifth-order polynomial.

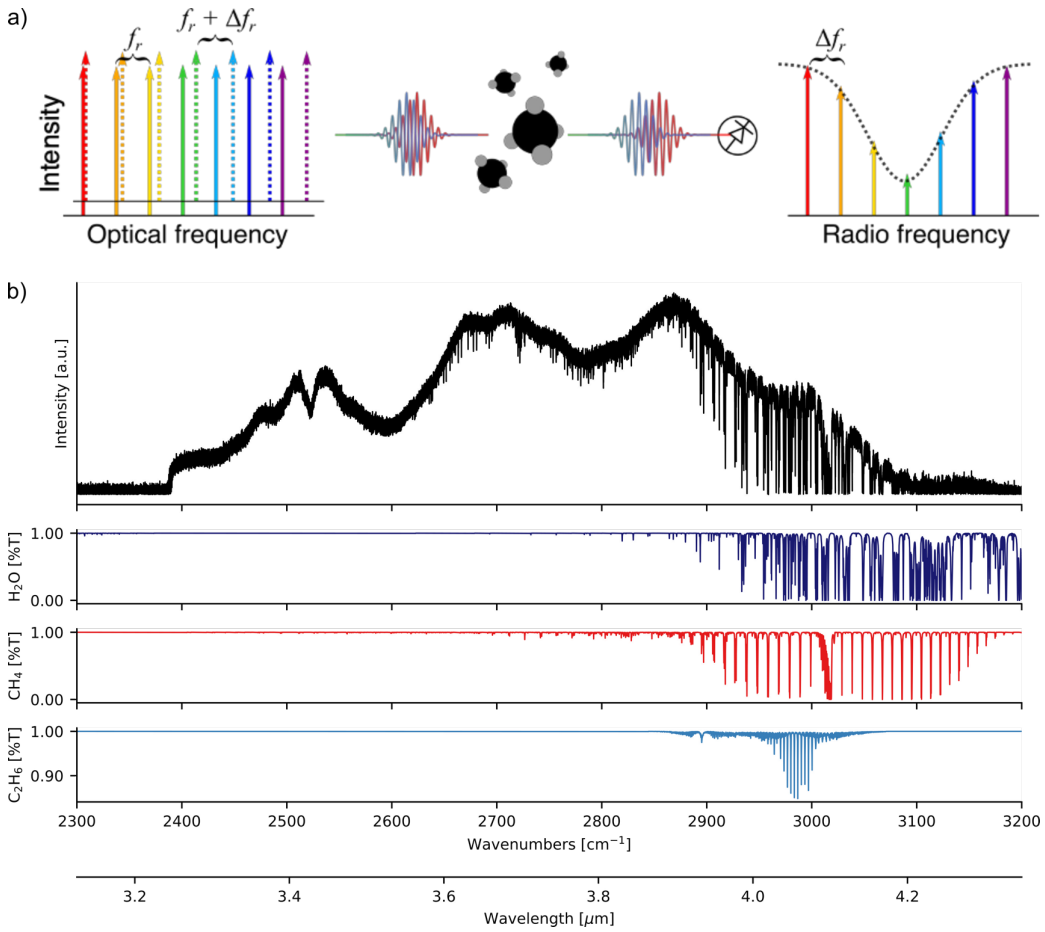

Figure S2. Mid-infrared dual-comb spectroscopy was used to measure methane, ethane, and water at PAO. a) A simplified diagram of the dual-comb spectroscopy technique. Two frequency combs with repetition rates $\boldsymbol{f_r}$ and $\boldsymbol{f_r + \Delta f}$ propagate along an open-air path. Molecules in the path absorb portions of the frequency comb light. The two combs then interfere on a detector, converting the optical comb and molecular absorption spectra to radio frequencies. b) A representative 2-minute averaged MIR spectrum for the PAO measurements (black trace). The overall shape is dominated by the comb spectra themselves, but the smaller sharp lines indicate transitions from multiple gas species. The lower graphs show the absorption spectra of water, methane, and ethane, scaled to the concentrations retrieved from the MIR spectrum on top.

Text S3: Inventory emissions from all sectors within this study's sensitivity area

Using the spatially gridded 2012 US EPA GHGI published by Maasakkers 2016, we calculate the integrated methane flux for each inventory sector within the sensitivity area of this study. The largest contributors are the energy and agriculture sectors, with landfills accounting for <1% of integrated methane flux.

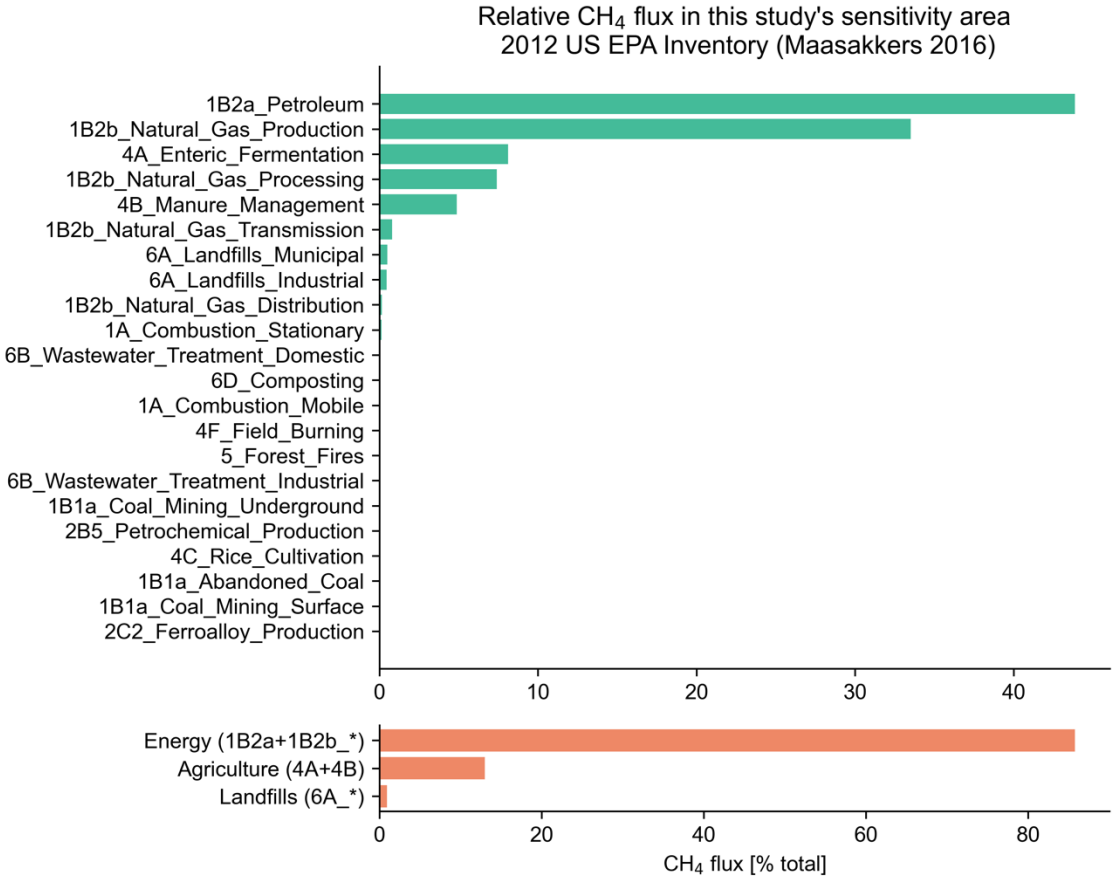

Figure S3. Relative individual (top) and grouped energy, agriculture, and landfill sector (bottom) methane fluxes integrated over this study's sensitivity area. Landfills contribute <1% of total methane flux.

Text S4: Dynamic linear model background estimation

A dynamic linear model tracer gas analysis is used to separate the observed methane time series into contributions from energy and agriculture emissions, and a background term:

$$[CH_4] = \beta_0 + \beta_1[C_2H_6] + \beta_2\,[NH_3] + \epsilon$$

In Northern Colorado, the β_0 term is the 'background' methane mixing ratio which would be measured in the absence of energy and agricultural methane emissions. To evaluate the plausibility of the β_0 values fit by the DLM, we compared data from PAO with data collected at two regional air quality monitoring sites shown in Figure S4a: Boulder Reservoir (BRZ) (Boulder County Public Health et al., n.d.) and Longmont Union Reservoir (LUR) (City of Longmont & Boulder A.I.R., LLC, n.d.).

While both BRZ and LUR measure methane and ethane concentrations, the lack of ammonia measurements at these sites precludes applying the tracer gas equation shown above. The background methane mixing ratio was instead defined as methane data recorded when the ethane concentration was <=5th percentile of the ethane time series. Background methane mixing ratios calculated using this approach are shown in the downward-going kernel density estimates in Figure S4b. The independently determined β_0 regression results from the DLM analysis (Figure S4b, upward-going kernel density estimate) overlapped with these three background estimates, indicating that the dynamic linear model tracer gas analysis provides a reasonable estimate of background conditions at PAO.

Because the background methane concentration is defined by the 5th percentile of the ethane data measured at each site, sites with elevated ethane concentrations (i.e., closer to more energy infrastructure) will also have elevated background methane concentrations. Indeed, Figure S4c demonstrates that background methane mixing ratios decreased linearly from PAO to LUR to BRZ as a function of well density.

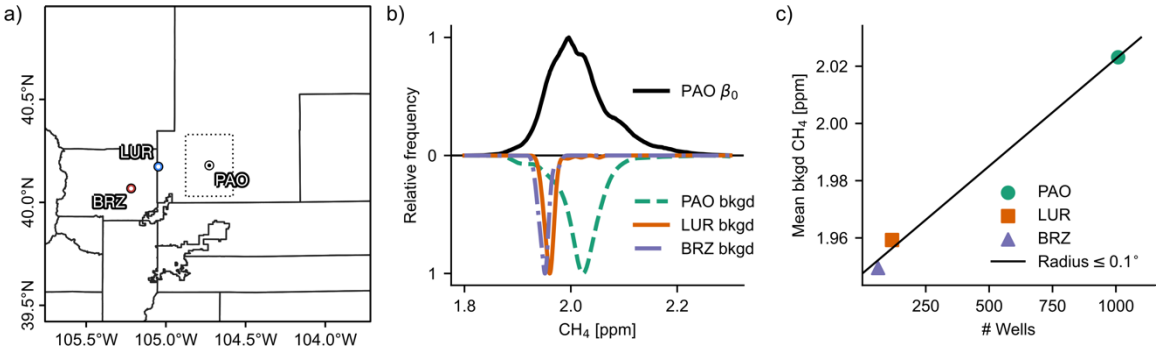

Figure S4. a) Methane and ethane mixing ratios measured at the Boulder Reservoir (BRZ) and Longmont Union Reservoir (LUR) air quality monitoring sites were used to independently estimate regional background methane mixing ratios. b) Background methane mixing ratios (defined as when the concentration of ethane was <=5th percentile of the ethane time series) measured at BRZ, LUR, and PAO ('PAO/LUR/BRZ bkgd') are consistent with the DLM analysis of the PAO data ('PAO $\boldsymbol{\beta_0}$'). c) Linear relationship between total number of wells within a given radius from each site and the background CH_4 concentration calculated for that site.

Text S5: Bayesian inverse analysis

A range of atmospheric dispersion simulations were run to determine the sensitivity of the transport matrix H to input parameters. Variability was assessed by performing simulations over a range of spatial resolutions (0.03° and 0.1°), back-trajectory durations (24 and 48 hours), numbers of particles (50, 100, and 200 particles), and with and without hyper-near field effects for a two-week period in November. Variations in y_{Energy}^{Prior} and y_{Agri}^{Prior} due to simulation inputs was found to be quite small compared to the estimated uncertainties specified in (Maasakkers et al., 2016) for x_{Energy}^{Prior} and x_{Agri}^{Prior}.

Using the observed sector-apportioned methane time series $\mathrm{y}^{\mathrm{Obs}}$, the 8-week hourly resolution transport matrix H, and emission inventories $\mathrm{x}^{\mathrm{Prior}}$, we generated optimized posterior inventories by calculating the maximum a posteriori (MAP) estimate $x^{Posterior}$ and posterior error covariance matrix $\hat{S}$ (Cusworth et al., 2020),

$$x^{Posterior} = x^{Prior} + SH^T(HSH^T + R)^{-1}(y^{Obs} - Hx^{Prior})$$

$$\hat{S} = (H^T R^{-1} H + S^{-1})^{-1}$$

Posterior solutions $x^{Posterior}$ and $\hat{S}$ require estimates for the observational error covariance matrix R and the prior error covariance matrix S, which are constructed as identity matrices multiplied by the respective scalar variances, σ_S and σ_R:

$$S = \sigma_S^2 I, \qquad R = \sigma_R^2 I$$

Both variances are determined using restricted maximum likelihood to find solutions $\theta = \{\sigma_R^2, \sigma_S^2\}$ that minimize the cost function (D. H. Cusworth et al., 2020; Michalak et al., 2005):

$$L_\theta = |HSH^T + R| + (Hx^{Prior} - y^{Obs})^T(HSH^T + R)^{-1}(Hx^{Prior} - y^{Obs})$$

From $\hat{S}$, we can calculate this study's averaging kernel matrix A:

$$A = I - \hat{S}S^{-1}$$

Posterior estimates are constrained by observations in regions where the diagonal elements of the averaging kernel are appreciably greater than 0. These diagonal elements (Figure S5) indicate that observations will constrain posterior emissions in a ~850 km^2 area centered around PAO. This "sensitivity area" is shown as a rectangular outline centered on PAO in the main text's Figures 3 and 4.

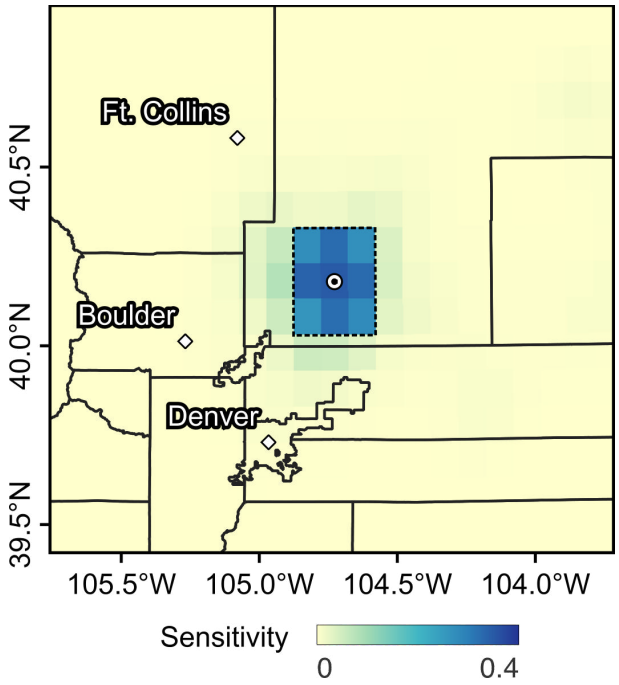

Figure S5. The diagonal elements of the averaging kernel sensitivity matrix A for observations at PAO. Posterior emissions are most strongly constrained by observations within a ~850 km^2 (0.3° × 0.3°) area centered around PAO (outlined in black dashed rectangle). The symmetric spatial distribution of A was conserved across sectors, although the degrees of freedom of signal (DOFS, the sum of the diagonal elements) changed slightly (Energy DOFS = 4.2, Agriculture DOFS = 3.6, Redistributed Agriculture DOFS = 4.8).

Inversion posteriors were evaluated on three metrics: the posterior's χ^2 metric, the relative reduction in root mean square error (RMSE) compared to the prior, and the relative increase in the coefficient of determination (R^2). χ^2 was calculated as (Kunik et al., 2019; Tarantola, 2005):

$$\chi^2 = \frac{1}{\nu}\left[(y^{Obs} - H\,\hat{x})^T R^{-1}(y^{Obs} - H\,\hat{x}) + (\hat{x} - x^{Prior})^T S^{-1}(\hat{x} - x^{Prior})\right]$$

Where ν is the degrees of freedom in the study, which in this case is equal to the number of independent observations in y^{Obs} (ν =238).

Reduction in root mean square error was calculated as:

$$\Delta RMSE\ [\%] = 100 \times \frac{(y^{Posterior} - y^{Obs}) - (y^{Prior} - y^{Obs})}{(y^{Prior} - y^{Obs})}$$

Similarly, the change in $R^2$was calculated as:

$$\Delta R^2\ [\%] = 100 \times \frac{R^2(y^{Posterior}, y^{Obs}) - R^2(y^{Prior}, y^{Obs})}{R^2(y^{Prior}, y^{Obs})}$$

The posterior fluxes and associated uncertainties depend upon the structure of the error covariance matrices. For this work, we chose to represent both the prior, S, and observational, R, error covariance matrices as diagonal matrices with uniform variances $\boldsymbol{\sigma}_R$ and $\boldsymbol{\sigma}_S$. To determine

appropriate $\boldsymbol{\sigma}_R$ and $\boldsymbol{\sigma}_S$ values, we first performed an ensemble of 100 inversions for each sector, where the variances were independently optimized using RML prior to each inversion. These error terms were then compared to the resulting posterior's χ^2 value to identify the range of covariance values which yielded an optimal estimate of the posterior given the prescribed variances ($\chi^2 \approx 1$). As shown in Figures S6-S8 for each sector below, the RML approach yields a wide range of observational ($\boldsymbol{\sigma}_R$, panels a)) and prior ($\boldsymbol{\sigma}_S$, panels b)) variances which follow a roughly inverse trend with χ^2. We also plot the posterior mean flux and mean uncertainty in the study's sensitivity area against χ^2 (panels c)). Mean fluxes were consistent across the full range of covariance estimates, with standard deviations approaching ~50% of the mean at around $\chi^2 = 1$.

Only a subset of the RML-derived variances are optimal, i.e, yield posterior solutions with $\chi^2 \approx 1$. A subsequent ensemble of 100 inversions were then performed for each sector using prior and observational variances uniformly sampled from a small interval around the range of $\boldsymbol{\sigma}_R$ and $\boldsymbol{\sigma}_S$ which yielded $\chi^2 \approx 1$. The mean and uncertainties of these posterior results are reported in the main paper.

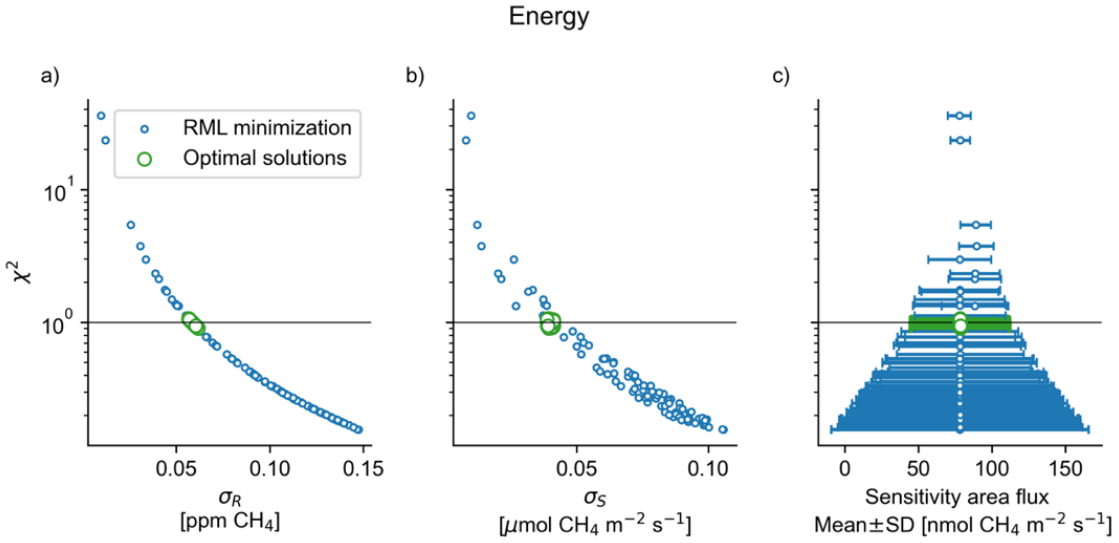

Figure S6. Energy sector restricted maximum likelihood estimates for $\boldsymbol{\sigma}_R$ (a) and $\boldsymbol{\sigma}_S$ (b) are compared to the resulting posterior's $\boldsymbol{\chi^2}$ score. Optimal errors are clustered around $\boldsymbol{\chi^2 \approx 1}$. Mean emissions within the study's sensitivity area (c) are largely independent of $\boldsymbol{\chi^2}$, although standard deviations are over-estimated when $\boldsymbol{\chi^2 \ll 1}$ and under-estimated when $\boldsymbol{\chi^2}$>>1.

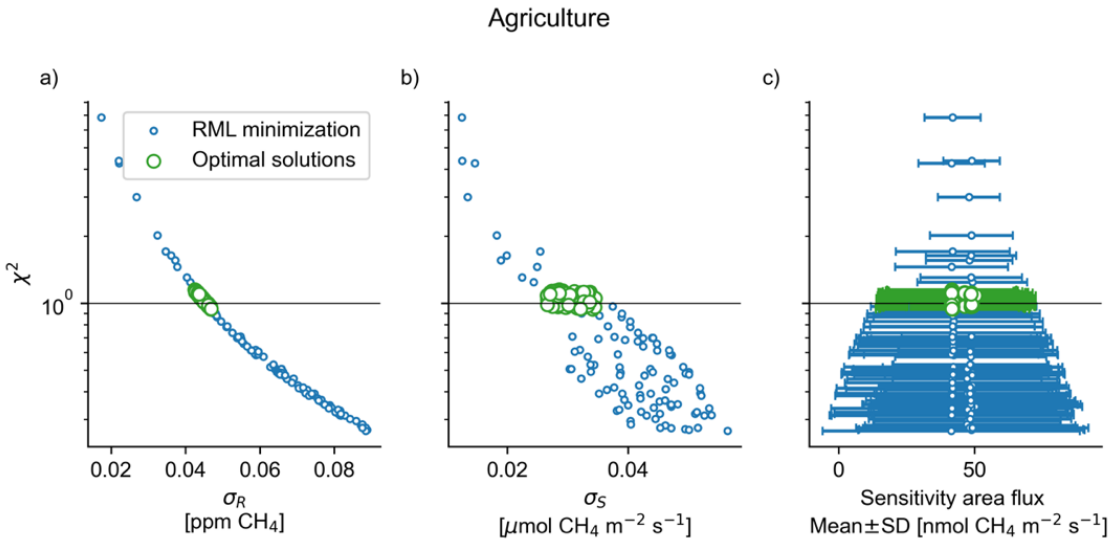

Figure S7. Same analysis as shown in Figure S6, but for the agriculture emissions inventory.

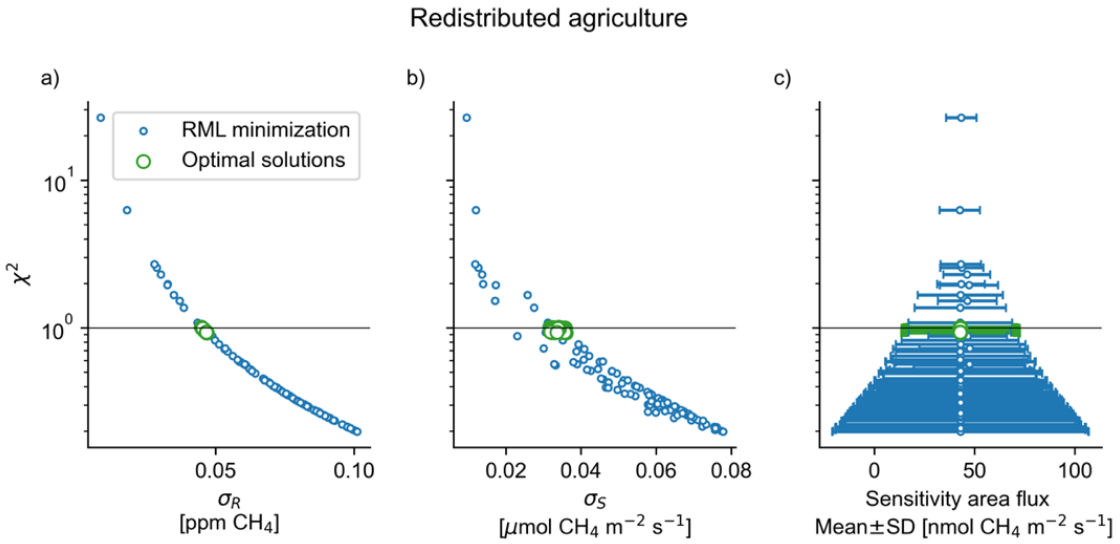

Figure S8. Same analysis as shown in Figures S6 and S7, but for the redistributed agriculture emissions inventory.

Text S6: Mean diurnal methane mixing ratios

Hourly mean (+/- SD) sector-apportioned observed (y^{Obs}) and predicted (y^{Prior}, $y^{Posterior}$) methane mixing ratios are shown in Figure S9. Energy sector mixing ratios are roughly consistent across observations and predictions. Both agriculture priors under-estimate agricultural methane.

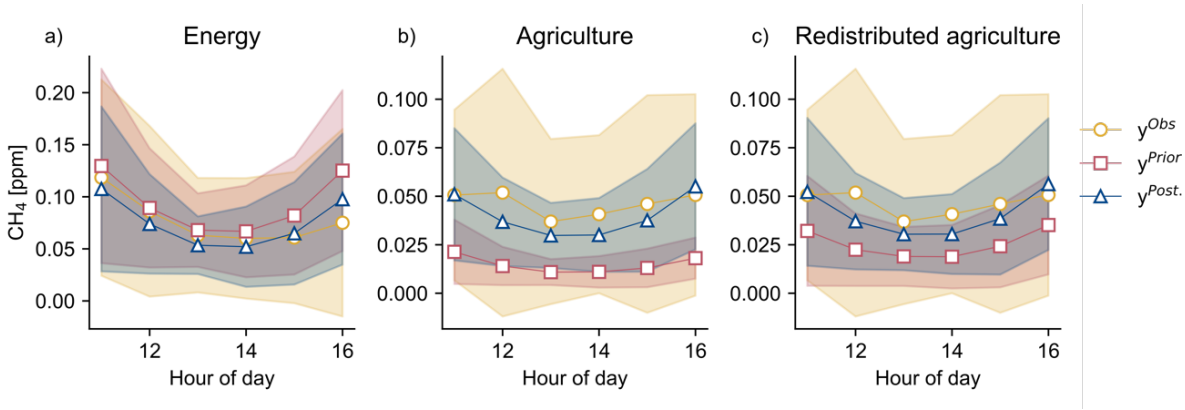

Figure S9. The hourly mean (+/- SD) observed, prior, and posterior methane mixing ratios from 11:00-16:00 local time are shown for each sector.

Text S7 Energy sector posterior sensitivity to a constant error in measured ethane concentrations

We estimate the effect of a constant +4 ppb offset (i.e. over-estimation of the ethane mixing ratio equal to the concentration measured at midday on Oct 31, 2021). To do so, the same dynamic linear model analysis described in the paper was performed with a 4 ppb offset subtracted from the raw ethane time series. The DLM calculation was performed 100 times. Next, a Bayesian inversion was performed for each of the 100 DLM results. In Table S2 we report the range of mean fluxes within the study's sensitivity area for the ensemble of 100 inversion results. This analysis demonstrates that the removal of a positive offset in retrieved ethane concentrations yields a smaller energy methane flux within the study's sensitivity area. However, as noted in Text S1, a multi-site comparison of ethane concentrations does not suggest an offset is present.

Table S2. Mean methane flux from the energy sector within the study's sensitivity area are shown below for two cases: 0 ppb ethane concentration offset (presented in the manuscript) and a 4 ppb offset which is subtracted from the ethane time series prior to dynamic linear model and inverse analyses. A hypothetical over-estimation of ethane concentrations, which is then removed by subtraction, ultimately yields a smaller methane flux attributed to the energy sector.

Ethane offset	Energy flux [nmol CH_4 m^{-2} s^{-1}]
0 ppb (manuscript value)	78 ± 3
4 ppb offset subtracted	63 ± 1

Text S8: Literature values for Northern Colorado energy sector methane fluxes

Multiple studies have estimated methane emissions from the Wattenberg Field using a variety of techniques, including aircraft mass balance, flask samples, and satellite inversions. These results are synthesized in Figure 3d to demonstrate the decadal decline in mean Wattenberg Field emissions factors. In Table S3, we present the data underlying that analysis, including the energy sector fluxes and associated uncertainties (in [Mg/hr]) derived by each study for the Wattenberg Field. We also provide the annual oil and gas production volumes (scaled to hourly barrels of oil equivalent) reported for the Field. By combining these two metrics, we estimate emissions factors for the Field as a function of time.

Barrels of oil equivalent production is calculated as the sum of the produced gas volume (in units of [MCF]), divided by 6, and the produced oil volume (in units of [BBL]).

Table S3 Literature values plotted in Figure 3d,e are provided in this table for reference.

Reference	Year	Production[10] [BOE/hr]	Flux [Mg/hr]	Flux σ [Mg/hr]	EF [kg CH4 / BOE]	EF σ [kg CH4 / BOE]
(Pétron et al., 2012)[1]	2008.58	6063.06	14.80	4.00	2.44	0.66
(Pétron et al., 2014)[2]	2012.42	8954.37	19.30	6.90	2.16	0.77
(Alvarez et al., 2018) [3]	2015.00	20632.61	21.00	2.00	1.02	0.10
(Peischl et al., 2018) [4]	2015.33	20632.61	18.00	8.00	0.87	0.39
(Shen et al., 2022) [5]	2018.00	29935.95	5.93	2.02	0.20	0.07
	2019.00	36464.27	5.93	2.02	0.16	0.06
	2020.00	36230.53	5.93	2.02	0.16	0.06
(Riddick et al., 2022)[6]	2021.58	33687.08	5.28	3.95	0.16	0.12
(Cusworth et al., 2022) [7]	2021.69	33687.08	15.23	4.06	0.45	0.12
(Fried & Dickerson, 2023)[8]	2021.83	33687.08	17.96	5.96	0.53	0.18
(Lu et al., 2022)[9]	2010.00	2818.76	13.25	2.67	4.70	0.95
	2011.00	3294.47	12.93	2.66	3.92	0.81
	2012.00	4117.12	9.86	1.93	2.40	0.47
	2013.00	5214.05	8.29	2.39	1.59	0.46
	2014.00	7278.48	8.83	2.14	1.21	0.29
	2015.00	9841.31	11.18	3.17	1.14	0.32
	2016.00	10677.75	8.23	2.50	0.77	0.23
	2017.00	11992.11	3.64	1.83	0.30	0.15
	2018.00	14989.69	4.44	2.53	0.30	0.17
	2019.00	17940.37	5.55	1.65	0.31	0.09
This work	2021.96	8953.33	3.85	1.64	0.43	0.18

Notes
[1] Table 4; flux from 129.6 Gg/yr; unc from mean difference between Top-Down Scenarios 1 and 2,3
[2] Table 1; flux +- unc from Average of Remaining balance
[3] Table S7 Bottom-up

[4] Table 1; estimated CH4 emissions from O&NG activity
[5] TROPOMI inversion; Table S1, 52 Gg/yr; 34% uncertainty from Section 3
[6] Using 37% O&NG for basin-wide emissions range of 125 (63-250) Gg CH4 / yr (see Discussion and Conclusion)
[7] Table 1 of Cusworth 2022; assume fraction of total sources which are O&NG is equal to the fraction of point sources which are O&NG; average of 19.91 Mg/hr and 10.55 Mg/hr results.
[8] Table 7; 71% of 25.3 +- 8.4 total CH4 emissions
[9] GOSAT inversion; Figure S5f
[10] Skinner 2022; barrel-of-oil equivalents (BOE) = Volume_oil [BBL] + Volume_gas [MCF]/6

Text S9: Wattenberg Field and sensitivity area infrastructure and production trends

We evaluate how representative this study's sensitivity area is relative to the larger Wattenberg Field using two metrics: new well installations and oil and gas production volumes. As shown in the top row of Figure S10, the study's sensitivity area encompasses a large fraction of the total new well installations and energy production in the Wattenberg Field. Relative trends in well installations and production volumes within the sensitivity area closely track the larger Field (bottom row, Figure S10). Thus, while this study does not directly measure the entire Wattenberg Field, applying this work's derived emissions factor to the entire Field (i.e., an extrapolation) is reasonable when comparing to other results from the literature.

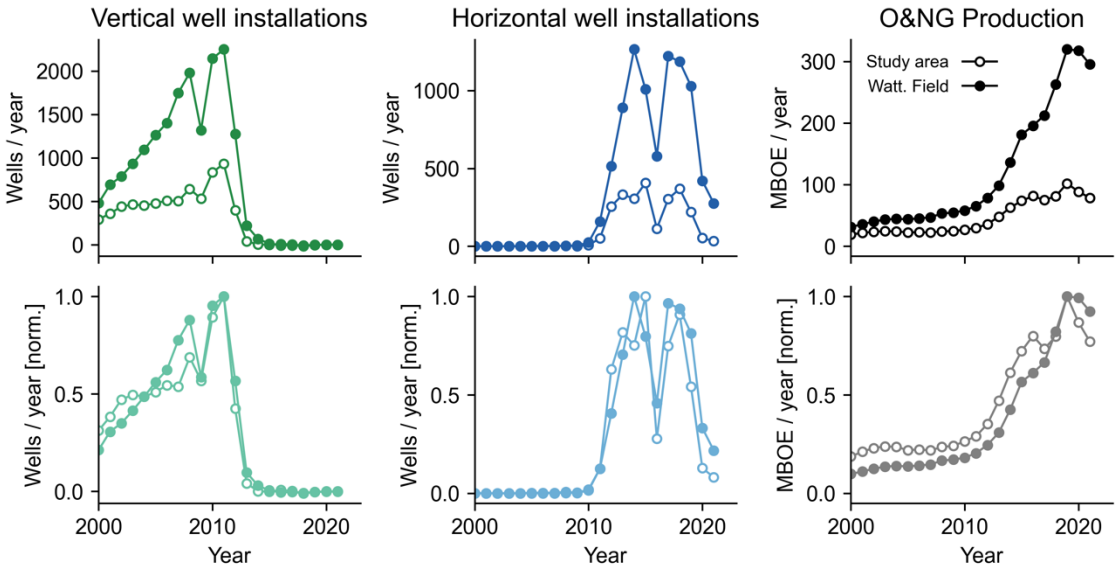

Figure S10. Time series of annual vertical and horizontal well installations, and oil and natural gas production, in the Wattenberg Field and this study's sensitivity area. Total installations and production are given in the top row, while the normalized values are shown on the bottom row. Both new well installations and energy production in this study's sensitivity area follow trends consistent with the larger Wattenberg Field.

Text S10: Redistributing agriculture methane emissions to CAFO locations

EPA agriculture emissions were redistributed to known CAFO locations using QGIS tools. First, the total emissions (4A+4B) for each county were calculated using the Zonal Statistics tool. This step reverses the probabilistic distribution of emissions throughout each county which was used to produce the EPA inventory. After exporting these county-level data to a comma separated variable format, the total emissions for each county were distributed to every CAFO within that county proportionate to the fractional animal equivalent units of livestock permitted at each CAFO (where 1 beef cattle = 0.7 dairy cattle = 10 swine = 100 poultry). This results in the same total agriculture emissions at the county level but spatially re-distributed to known CAFO locations according to relative CAFO size and primary livestock type. CAFO distributed emissions data were then re-imported to QGIS; after generating a 0.1° grid with the same spatial extent as the EPA inventory, the total emissions per grid element was calculated using the Points in Polygon query. Finally, the emissions were converted to a raster and exported as a netCDF file, producing an updated AG emissions inventory with the same extent and resolution as the original EPA inventory. (This redistributed inventory only defines emissions within the state of Colorado.)

Alvarez, R. A., Zavala-Araiza, D., Lyon, D. R., Allen, D. T., Barkley, Z. R., Brandt, A. R., et al. (2018). Assessment of methane emissions from the U.S. oil and gas supply chain. *Science*, 186–188. https://doi.org/10.1126/science.aar7204

Benjamin, S. G., Weygandt, S. S., Brown, J. M., Hu, M., Alexander, C. R., Smirnova, T. G., et al. (2016). A North American Hourly Assimilation and Model Forecast Cycle: The Rapid Refresh. *Monthly Weather Review*, *144*(4), 1669–1694. https://doi.org/10.1175/MWR-D-15-0242.1

Boulder County Public Health, Boulder A.I.R., LLC, & Colorado Department of Public Health and Environment. (n.d.). Boulder Reservoir Atmospheric Chemical Conditions. Retrieved from https://www.bouldair.com/boulder.htm#header

City of Longmont, & Boulder A.I.R., LLC. (n.d.). Longmont Union Reservoir Atmospheric Chemical Conditions. Retrieved from https://www.bouldair.com/longmont.htm

Cusworth, D., Thorpe, A., Ayasse, A., Stepp, D., Heckler, J., Asner, G., et al. (2022). *Strong methane point sources contribute a disproportionate fraction of total emissions across multiple basins in the U.S.* (preprint). Earth Sciences. https://doi.org/10.31223/X53P88

Cusworth, D. H., Duren, R. M., Yadav, V., Thorpe, A. K., Verhulst, K., Sander, S., et al. (2020). Synthesis of Methane Observations Across Scales: Strategies for Deploying a Multitiered Observing Network. *Geophysical Research Letters*, *47*(7). https://doi.org/10.1029/2020GL087869

Fried, A., & Dickerson, R. R. (2023). *Continuous Airborne Measurements and Analysis of Oil & Natural Gas Emissions During the 2021 Denver-Julesburg Basin Studies*. University of Colorado Boulder. Retrieved from https://apcd.state.co.us/aqidev/tech_doc_repository.aspx?action=open&file=CU_UMD_2021_Final_Report.pdf

Giorgetta, F. R., Peischl, J., Herman, D. I., Ycas, G., Coddington, I., Newbury, N. R., & Cossel, K. C. (2021). Open-Path Dual-Comb Spectroscopy for Multispecies Trace Gas Detection in the 4.5–5 μm Spectral Region. *Laser & Photonics Reviews*, *15*(9), 2000583. https://doi.org/10.1002/lpor.202000583

Gordon, I. E., Rothman, L. S., Hargreaves, R. J., Hashemi, R., Karlovets, E. V., Skinner, F. M., et al. (2021). The HITRAN2020 molecular spectroscopic database. *Journal of Quantitative Spectroscopy and Radiative Transfer*, 107949. https://doi.org/10.1016/j.jqsrt.2021.107949

Gordon, I. E., Rothman, L. S., Hargreaves, R. J., Hashemi, R., Karlovets, E. V., Skinner, F. M., et al. (2022). The HITRAN2020 molecular spectroscopic database. *Journal of Quantitative Spectroscopy and Radiative Transfer*, *277*, 107949. https://doi.org/10.1016/j.jqsrt.2021.107949

Herman, D., Mead, G., Giorgetta, F. R., Baumann, E., Malarich, N., Washburn, B. R., et al. (2023). Open-path measurement of stable water isotopologues using mid-infrared dual-comb spectroscopy.

Kunik, L., Mallia, D. V., Gurney, K. R., Mendoza, D. L., Oda, T., & Lin, J. C. (2019). Bayesian inverse estimation of urban CO2 emissions: Results from a synthetic data simulation over Salt Lake City, UT. *Elementa: Science of the Anthropocene*, *7*, 36. https://doi.org/10.1525/elementa.375

Lu, X., Jacob, D. J., Wang, H., Maasakkers, J. D., Zhang, Y., Scarpelli, T. R., et al. (2022). Methane emissions in the United States, Canada, and Mexico: evaluation of national methane emission inventories and 2010–2017 sectoral trends by inverse analysis of in situ (GLOBALVIEWplus CH₄ ObsPack) and satellite (GOSAT) atmospheric observations. *Atmospheric Chemistry and Physics*, *22*(1), 395–418. https://doi.org/10.5194/acp-22-395-2022

Maasakkers, J. D., Jacob, D. J., Sulprizio, M. P., Turner, A. J., Weitz, M., Wirth, T., et al. (2016). Gridded National Inventory of U.S. Methane Emissions. *Environmental Science & Technology*, *50*(23), 13123–13133. https://doi.org/10.1021/acs.est.6b02878

Michalak, A. M., Hirsch, A., Bruhwiler, L., Gurney, K. R., Peters, W., & Tans, P. P. (2005). Maximum likelihood estimation of covariance parameters for Bayesian atmospheric trace gas surface flux inversions. *Journal of Geophysical Research*, *110*(D24), D24107. https://doi.org/10.1029/2005JD005970

Newville, Matthew, Stensitzki, Till, Allen, Daniel B., & Ingargiola, Antonino. (2014, September 21). LMFIT: Non-Linear Least-Square Minimization and Curve-Fitting for Python. Zenodo. https://doi.org/10.5281/zenodo.11813

Peischl, J., Eilerman, S. J., Neuman, J. A., Aikin, K. C., de Gouw, J., Gilman, J. B., et al. (2018). Quantifying Methane and Ethane Emissions to the Atmosphere From Central and Western U.S.

Oil and Natural Gas Production Regions. *Journal of Geophysical Research: Atmospheres*. https://doi.org/10.1029/2018JD028622

Pétron, G., Frost, G., Miller, B. R., Hirsch, A. I., Montzka, S. A., Karion, A., et al. (2012). Hydrocarbon emissions characterization in the Colorado Front Range: A pilot study: COLORADO FRONT RANGE EMISSIONS STUDY. *Journal of Geophysical Research: Atmospheres*, *117*(D4), n/a-n/a. https://doi.org/10.1029/2011JD016360

Pétron, G., Karion, A., Sweeney, C., Miller, B. R., Montzka, S. A., Frost, G. J., et al. (2014). A new look at methane and nonmethane hydrocarbon emissions from oil and natural gas operations in the Colorado Denver-Julesburg Basin. *Journal of Geophysical Research: Atmospheres*, *119*(11), 6836–6852. https://doi.org/10.1002/2013JD021272

Riddick, S. N., Cheptonui, F., Yuan, K., Mbua, M., Day, R., Vaughn, T. L., et al. (2022). Estimating Regional Methane Emission Factors from Energy and Agricultural Sector Sources Using a Portable Measurement System: Case Study of the Denver–Julesburg Basin. *Sensors*, *22*(19), 7410. https://doi.org/10.3390/s22197410

Roy, J., Deschênes, J.-D., Potvin, S., & Genest, J. (2012). Continuous real-time correction and averaging for frequency comb interferometry. *Optics Express*, *20*(20), 21932–21939. https://doi.org/10.1364/OE.20.021932

Shen, L., Gautam, R., Omara, M., Zavala-Araiza, D., Maasakkers, J. D., Scarpelli, T. R., et al. (2022). Satellite quantification of oil and natural gas methane emissions in the US and Canada including contributions from individual basins. *Atmospheric Chemistry and Physics*, *22*(17), 11203–11215. https://doi.org/10.5194/acp-22-11203-2022

Tarantola, A. (2005). *Inverse Problem Theory and Methods for Model Parameter Estimation*. Society for Industrial and Applied Mathematics. https://doi.org/10.1137/1.9780898717921

Ycas, G., Giorgetta, F. R., Baumann, E., Coddington, I., Herman, D., Diddams, S. A., & Newbury, N. R. (2018). High-coherence mid-infrared dual-comb spectroscopy spanning 2.6 to 5.2 μm. *Nature Photonics*, *12*(4), 202–208. https://doi.org/10.1038/s41566-018-0114-7

Ycas, G., Giorgetta, F. R., Cossel, K. C., Waxman, E. M., Baumann, E., Newbury, N. R., & Coddington, I. (2019). Mid-infrared dual-comb spectroscopy of volatile organic compounds across long open-air paths. *Optica*, *6*(2), 165–168. https://doi.org/10.1364/OPTICA.6.000165

Ycas, G., Giorgetta, F. R., Friedlein, J. T., Herman, D., Cossel, K. C., Baumann, E., et al. (2020). Compact mid-infrared dual-comb spectrometer for outdoor spectroscopy. *Optics Express*, *28*(10), 14740–14752. https://doi.org/10.1364/OE.385860